**Advances in Materials Research,** *Vol. 15, No. 1 (2026) 23-47*
https://doi.org/10.12989/amr.2026.15.1.023

Techno-Press

# Management of nonlinear waves in solar cells: Results verification through DNN–GA framework

Suleiman Ibrahim Mohammad[1], Asokan Vasudevan[2,3], Wan Mohd Hirwani Wan Hussain*[4], Basem Abu Zneid[5]

[1]*Research follower, INTI International University, 71800 Negeri Sembilan, Malaysia*
[2]*Faculty of Business and Communications, INTI International University, 71800 Negeri Sembilan, Malaysia*
[3]*Shinawatra University, 99 Moo 10, Bangtoey, Samkhok, Pathum Thani 12160 Thailand*
[4]*Graduate School of Business, Universiti Kebangsaan Malaysia, Bangi,43600, Selangor, Malaysia*
[5]*Faculty of Engineering, Hourani Center for Applied Scientific Research, Al-Ahliyya Amman University, Amman, Jordan*

*(Received September 24, 2025, Revised December 25, 2025, Accepted January 5, 2026)*

**Abstract.** Management of nonlinear wave propagation in graphene-reinforced solar cells is an important part of their performance improvement and reliability. In this paper, the authors examine the nonlinear phase velocity characteristics of graphene-reinforced composite materials in the case of micro-sized solar cell plates. They use a new deep neural network-genetic algorithm (DNN–GA) combination to check the nonlinear wave propagation results, thereby increasing the prediction's accuracy and efficiency. The Halpin-Tsai model is used for determining the effective properties of graphene-reinforced composites, whereas the modified coupled stress theory (MCST) and sinusoidal shear deformation theory (SSDT) are combined to reflect the influence of microstructural behaviors on wave propagation. Modified pair stress theory (MPST) is also used to allow for the size-dependent and microstructural deformation effects of the composite material. The governing equations are obtained through Hamilton's principle, and an analytical method is then used to find the solutions to these equations. The results reveal that graphene reinforcement has a significant effect on the phase velocity and that the proposed framework is very useful for accurately tracing the material's nonlinear dynamical states. The research has pointed out the fact that it is critical to resort to effective management methods so that the nonlinear wave propagation can be controlled in order to sustain the micro-sized solar cells' structural integrity and performance enhancement in real-life applications. Now, this framework has become a reliable instrument for designing and optimizing advanced graphene-reinforced composites, which are meant for the next generation of solar technologies.

**Keywords:** DNN–GA; graphene-reinforced composites; management; modified coupled stress theory; nonlinear wave propagation; solar cell optimization

## 1. Introduction

The role of solar cells in modern engineering is significant because they can supply clean and renewable energy [1,2]. The world is transitioning to sustainable methods, and the engineers' efforts in developing solar power technologies with high efficiency are the main reason for the

*Corresponding author, Ph.D., E-mail: wmhwh@ukm.edu.my



ISSN: 2234-0912 (Print), 2234-179X (Online)

reduction of fossil fuel consumption [3]. Besides, solar cells are the source of innovations in different sectors such as transportation, construction, and electronics [4]. Engineers who know solar cell technology can easily tackle global challenges like climate change and energy shortage [5]. Thus, knowledge of solar cells is becoming a must-have for engineers who are committed to the sustainability of the future [6].

The investigation of nonlinear guided wave propagation for solar cells stacked in multilayers is not just an academic exercise but a key method for monitoring the condition (SHM) and evaluating the structure without damage (NDE). In the case of aerospace applications, where the costs of maintenance are extremely high, the capacity to reveal very early damage, such as micro-cracks, delamination between layers, or deterioration of properties due to fatigue, is most important. Nonlinear guided waves are extremely good at picking up such minor changes and faults inside the material, thus, the potential to perform in-situ assessments of the mechanical integrity of solar cells. The ability to understand their propagation characteristics is, therefore, a means to directly determine the reliability of the structure and the remaining life of the energy-generating component, hence, making it possible to draw a direct connection between mechanical waves and the sustainability of performance in terms of the life of the solar cell.

The efficiency and stability of silicon solar cells have made them unavoidable in the area of photovoltaics [7,8]. Silicon is the most preferred material for the fabrication of solar panels because of its high efficiency and low cost [9]. This element is also one of the most abundant minerals; thus, it guarantees that the supply for large-scale electricity generation to be large-scale is both sustainable and scalable [10]. The great production methods of silicon wafers that have been developed over the years lead to lower costs and a more uniform quality output [11]. The new technological developments with silicon cells, such as PERC (passivated emitter and rear cell) have been a major factor in their improvement in energy conversion effectiveness [12]. Also, their ability to adapt to different installation surroundings has opened up the areas of use for homes, businesses, and utility companies [13]. Silicon-based photovoltaics play a key role in the accomplishment of global renewable energy goals and the mitigation of greenhouse gas emissions [14]. The extensive use of silicon solar cells has also pushed forward the research of new materials and the tandem cell structures [15]. In conclusion, silicon solar cells are still the mainstay of solar energy technology and a driving force to a sustainable energy future [16].

The analysis of stability is a primary tool of the engineer's trade, and it is a prerequisite for the safety and reliability assessment of any structure, system, or process [17]. These engineers are able to forecast the behavior of a system under various disturbances or changes in operating conditions [18]. Inaccurate stability analysis can lead to catastrophic failures, in forms of structural collapses or uncontrolled system behaviors, among others [19]. By knowing the limits of stability, engineers can come up with designs that are able to cope with both normal and extreme conditions, thus securing the resources and materials required to carry out the stay effectively hence making the product more economical and environmentally friendly [20]. Stability analysis is indispensable across various engineering disciplines including civil, mechanical, electrical, and aerospace [21]. The engineer is provided with the means to meet the industry's standards, regulations, and safety codes through stability analysis [22]. Potential design errors can be detected by engineers in the early stages of the development process through stability assessment [23]. These preventive measures not only save money on maintenance costs but also prolong the lifetime of engineering systems [24]. In the end, stability analysis remains a necessity in the quest for innovations, professional efficiency, and the building of public confidence in engineering tenets and projects [25].

Across the board, machine learning is now a necessity that is primarily used to make accurate predictions in the fields of engineering, finance, and healthcare [26]. It can process huge data sets and do so with much better speed and efficiency compared to the traditional methods of statistics [27]. By being trained on past data, machine learning models are able to recognize the complex patterns and relationships that human analysts might not catch [28]. This forecasting ability allows for the early detection of trends, anomalies, or risks, which in turn, supports the organizations to make timely and efficient decisions [29]. The good thing about machine learning is that it can learn new things, hence, it gets better at making predictions over time as more data comes in [30]. And it does so effectively, without human involvement, thus, reducing errors, and bringing about higher productivity [31]. The engineering field, in particular, is one of the places where machine learning finds application in areas such as predictive maintenance, quality control, and design optimization [32].

For the very first time, nonlinear wave propagation management in solar cells with graphene reinforcement is opened up to the exploitation of a powerful DNN-GA framework. The nonlinear phase velocity changingnon-the-fleeting-micro-plates-what-is-here-reinforced-with-graphene behavior, under various loading conditions, is verified by the innovative method. The Halpin-Tsai model is used to predict the properties of the composite material combination very effectively, while the modified coupled stress theory and sinusoidal shear deformation theory are integrated to properly reflect the influence of microstructural behavior on wave dynamics. The modified pair stress theory is applied to capture the size-dependent effects, and in turn, Hamilton's principle is employed to derive the governing equations of motion. An analytical method is used to solve the governing equations, and the results indicate that the suggested framework has a considerable impact on the prediction accuracy of nonlinear wave propagation in composites based on graphene. The revelations imply that new strategies for the control of nonlinearity in wave lifetimes and the fine-tuning of solar cell plates for the best combination of mechanical performance and energy conversion efficiency have been discovered. This cutting-edge method is especially significant in the context of next-generation solar cells that are ultra-efficient and stylish where the interrelationship of the variables like material and wave dynamics being micromanaged is paramount to renewable energy technologies' advancements. A comprehensive and trustworthy tool for graphene-imported solar cell innovation in the future is thus outlined by the research.

## 2. Mathematical modeling

Fig. 1 shows a cross-section of a solar cell that is made of several layers and has been reinforced with graphene, with the focus being on the arrangement of the materials in layers. The model presents the solar cell different layers' construction, and each layer is identified by a specific label related to its physical characteristics and its function. The layer on the very top, having the label "top metal contact," is the collection point for the electric current since it is the conductive surface. Underneath, the "anti-reflective coating" ($h_7$) is applied to reduce the light that is lost, thus, increasing the efficiency of the cell. The "transparent conductive oxide" ($h_3$) layer makes light penetration its priority, while at the same time, it is allowing the current to flow. The layers below consist of the "N-type silicon layer" ($h_5$), "intrinsic (i-layer) silicon" ($h_4$), and "P-type silicon layer" ($h_3$), which contribute to the generation of the photovoltaic effect. These layers are necessary for the solar cell to function, with the intrinsic silicon layer being the most important middle layer for charge separation. The "back reflector" ($h_2$) increases the amount of light that is

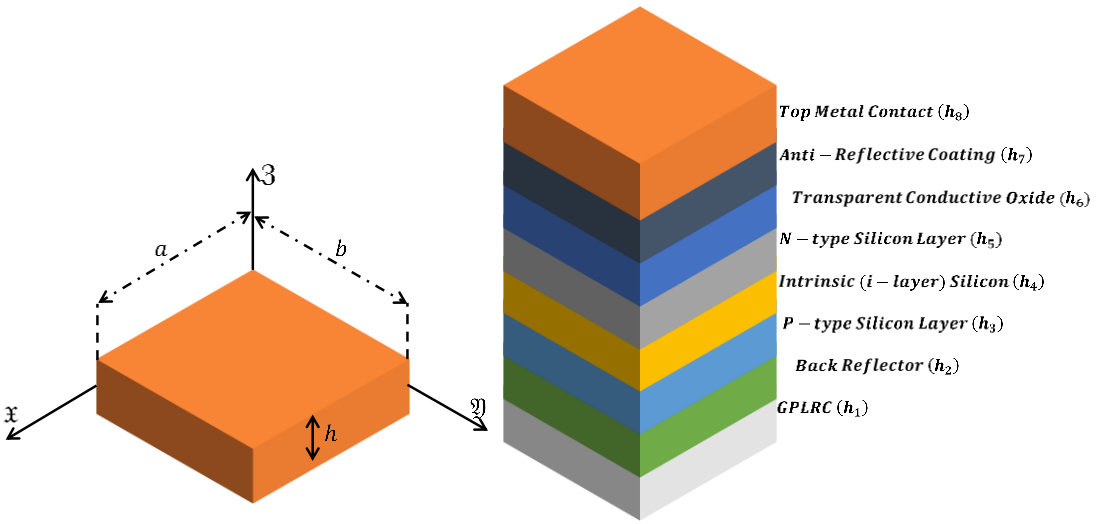


Figure 1. A cross-section of a solar cell that is made of several layers and has been reinforced with graphene, with the focus being on the arrangement of the materials in layers

absorbed by the solar cell through its reflection of light escaping from the other layers, thus, increasing the absorption rate. The "GPLRC" ($h_1$) layer, in turn, shows the graphene-reinforced composite material that strengthens the solar cell both mechanically and electrically, thus, making it less fragile and more efficient in controlling the nonlinear wave propagation. This arrangement is crucial for the analysis done with the DNN-GA framework, which makes it possible to assess the nonlinear wave propagation in the ecosystem of the graphene-reinforced solar cell, thereby, improving the performance and also the reliability of the device.

## 2.1 Material properties

The transverse dispersion of GPLs is simulated using three distinct patterns, as shown in Fig. 2. Using a modified version of the Halpin-Tsai correlation, the following formula was derived to find the GPLR nanocomposite material's effective elastic modulus [33]:

$$E_c(3) = -\frac{3}{8}\frac{1+\xi_L\eta_L V_{GPL}}{\eta_L V_{GPL}-1}\times E_m - \frac{5}{8}\frac{1+\xi_W\eta_W V_{GPL}}{\eta_W V_{GPL}-1}\times E_m \tag{1}$$

where $\xi_L = 2\frac{L_{GPL}}{t_{GPL}}$, $\xi_W = 2\frac{g_{GPL}}{t_{GPL}}$, $V^*_{GPL} = \frac{g_{GPL}}{\left(\frac{\rho_{GPL}}{\rho_m}\right)(1-g_{GPL})+g_{GPL}}$, $\eta_W = -\frac{1-\left(\frac{E_{GPL}}{E_m}\right)}{\xi_W+\left(\frac{E_{GPL}}{E_m}\right)}$, and $\eta_L = \frac{\left(\frac{E_{GPL}}{E_m}\right)-1}{\left(\frac{E_{GPL}}{E_m}\right)+\xi_L}$. The law of mixtures would be used to determine the composite plate's effective mass density and Poisson's ratio [34]:

$$\begin{aligned}\rho_c(3) &= \rho_{GPL}V_{GPL} + \rho_m(1-V_{GPL}),\\ \nu_c(3) &= \nu_{GPL}V_{GPL} + \nu_m(1-V_{GPL}).\end{aligned} \tag{2}$$

Although the definition of the effective shear modulus is [35]

Table 1. The shape and material properties of the metal layer, as well as the GPL-reinforced nanocomposite (effective properties)

| Source | Symbol | Value | Unit |
|---|---|---|---|
| GPL | $v_{GPL}$ | 0.186 | – |
| | $\rho_{GPL}$ | $1.06 \times 10^3$ | $kg/m^3$ |
| | $E_{GPL}$ | $1.01 \times 10^9$ | $Pa$ |
| | $l_{GPL}$ | $2.5 \times 10^{-6}$ | $m$ |
| | $w_{GPL}$ | $1.5 \times 10^{-6}$ | $m$ |
| | $t_{GPL}$ | $1.5 \times 10^{-9}$ | $m$ |
| Aluminum epoxy (matrix) | $v_m$ | 0.35 | – |
| | $\rho_m$ | 2601 | $kg/m^3$ |
| | $E_m$ | $70 \times 10^9$ | $Pa$ |

$$G_c(\mathfrak{Z}) = \frac{E_c(\mathfrak{Z})}{2(1+\nu_c(\mathfrak{Z}))} \tag{3}$$

The analytical expressions of these patterns are as follows

$$\begin{aligned} &\text{GPL-X: } V_{GPL} = 4V^*_{GPL}\frac{\left|\mathfrak{Z}+\frac{h}{2}-\frac{h_1}{2}\right|}{h_1}, \\ &\text{GPL-O: } V_{GPL} = 2V^*_{GPL}\left(1-2\frac{\left|\mathfrak{Z}+\frac{h}{2}-\frac{h_1}{2}\right|}{h_1}\right), \\ &\text{GPL-UD: } V_{GPL} = V^*_{GPL}. \end{aligned} \tag{4}$$

where $\mathfrak{Z} = \frac{(k-1)h_1}{N_L-1} - \frac{h}{2}$, $k = 1, \ldots, N_L$.

The properties of the materials utilized are listed in Table 1. The homogenized property of the GPL-reinforced aluminum epoxy nanocomposite layer is represented by the effective elastic modulus shown in Table 1, which was computed using the Halpin-Tsai model in Eq. (1) and is compatible with the scale and filler content used in this investigation [33, 34]. This is not the same as pure graphene's intrinsic modulus, which is usually about 1 TPa.

An overview of the properties of the materials used to make the modern, improved silicon solar cells is also given in Table 2.

## 2.2 Kinematic relations

In this paper, the micro-sized plate under study is assumed. Fig. 1 shows that the lattice plate has dimensions of $h$ for thickness and $a$, and $b$ for length and width. In this study, the improved silicon solar cell is mechanically analyzed utilizing sinusoidal shear deformation theory and modified couple stress theory. The displacement components of the specified improved silicon solar cell may be described as follows using the sinusoidal shear deformation theory (SSDT):

Table 2. An inventory of the characteristics of the components used to create the more sophisticated, modern silicon solar cells [36]

| Layer | Material | $h$ | $E$ | $\rho$ | $\nu$ |
|---|---|---|---|---|---|
| 1 | GPLRC | 50 [μ$m$] | $E_c$ | $\rho_c$ | $\nu_c$ |
| 2 | Back Reflector | 350 [$nm$] | 69 [$GPa$] | 2700 | 0.33 |
| 3 | P-type Silicon Layer | 5 [μ$m$] | 75 [$GPa$] | 2330 | 0.3 |
| 4 | Intrinsic (i-layer) Silicon | 250 [$nm$] | 75 [$GPa$] | 2330 | 0.3 |
| 5 | N-type Silicon Layer | 35 [$nm$] | 75 [$GPa$] | 2330 | 0.3 |
| 6 | Transparent Conductive Oxide | 200 [$nm$] | 120 [$GPa$] | 7140 | 0.25 |
| 7 | Anti-Reflective Coating | 70 [$nm$] | 200 [$GPa$] | 3170 | 0.28 |
| 8 | Top Metal Contact | 150 [$nm$] | 83 [$GPa$] | 10490 | 0.37 |

$$\mathfrak{u}(\mathfrak{X},\mathfrak{Y},\mathfrak{Z},\mathfrak{T}) = \mathfrak{u}_0(\mathfrak{X},\mathfrak{Y},\mathfrak{T}) - \mathfrak{Z}\frac{\partial \mathfrak{w}_0(\mathfrak{X},\mathfrak{Y},\mathfrak{T})}{\partial \mathfrak{X}} + \frac{h}{\pi} sin\left(\frac{\pi \mathfrak{Z}}{h}\right)\left(\frac{\partial \mathfrak{w}_0(\mathfrak{X},\mathfrak{Y},\mathfrak{T})}{\partial \mathfrak{X}} - \mathfrak{S}_{\mathfrak{X}}(\mathfrak{X},\mathfrak{Y},\mathfrak{T})\right), \tag{5a}$$

$$\mathfrak{v}(\mathfrak{X},\mathfrak{Y},\mathfrak{Z},\mathfrak{T}) = \mathfrak{v}_0(\mathfrak{X},\mathfrak{Y},\mathfrak{T}) - \mathfrak{Z}\frac{\partial \mathfrak{w}_0(\mathfrak{X},\mathfrak{Y},\mathfrak{T})}{\partial \mathfrak{Y}} + \frac{h}{\pi} sin\left(\frac{\pi \mathfrak{Z}}{h}\right)\left(\frac{\partial \mathfrak{w}_0(\mathfrak{X},\mathfrak{Y},\mathfrak{T})}{\partial \mathfrak{Y}} - \mathfrak{S}_{\mathfrak{Y}}(\mathfrak{X},\mathfrak{Y},\mathfrak{T})\right), \tag{5b}$$

$$\mathfrak{w}(\mathfrak{X},\mathfrak{Y},\mathfrak{Z},\mathfrak{T}) = \mathfrak{w}_0(\mathfrak{X},\mathfrak{Y},\mathfrak{T}). \tag{5c}$$

where $\mathfrak{v}$, and $\mathfrak{w}$ are the $\mathfrak{X}$-, $\mathfrak{Y}$-, and $\mathfrak{Z}$-components of the displacement vector, and $\mathfrak{S}_{\mathfrak{X}}$ and $\mathfrak{S}_{\mathfrak{Y}}$ are the angles of rotation of the cross sections around the y and x axes at any point on the microplate's mid-plane, respectively. Furthermore, the microplate's mid-plane displacements in the $\mathfrak{X}$-, $\mathfrak{Y}$-, and $\mathfrak{Z}$-axes are denoted by $\mathfrak{u}_0$, $\mathfrak{v}_0$ and $\mathfrak{w}_0$. According to the introduced displacement, the strain components are shown as [37].

$$\mathfrak{E}_{\mathfrak{X}\mathfrak{X}} = \frac{\partial \mathfrak{u}(\mathfrak{X},\mathfrak{Y},\mathfrak{Z},\mathfrak{T})}{\partial \mathfrak{X}} + \frac{1}{2}\left(\frac{\partial \mathfrak{w}(\mathfrak{X},\mathfrak{Y},\mathfrak{Z},\mathfrak{T})}{\partial \mathfrak{X}}\right)^2, \tag{6a}$$

$$\mathfrak{E}_{\mathfrak{Y}\mathfrak{Y}} = \frac{\partial \mathfrak{v}(\mathfrak{X},\mathfrak{Y},\mathfrak{Z},\mathfrak{T})}{\partial \mathfrak{Y}} + \frac{1}{2}\left(\frac{\partial \mathfrak{w}(\mathfrak{X},\mathfrak{Y},\mathfrak{Z},\mathfrak{T})}{\partial \mathfrak{Y}}\right)^2, \tag{6b}$$

$$\mathfrak{E}_{\mathfrak{X}\mathfrak{Y}} = \frac{1}{2}\frac{\partial}{\partial \mathfrak{X}}\mathfrak{v}(\mathfrak{X},\mathfrak{Y},\mathfrak{Z},\mathfrak{T}) + \frac{1}{2}\frac{\partial}{\partial \mathfrak{Y}}\mathfrak{u}(\mathfrak{X},\mathfrak{Y},\mathfrak{Z},\mathfrak{T}) + \frac{1}{2}\frac{\partial \mathfrak{w}(\mathfrak{X},\mathfrak{Y},\mathfrak{Z},\mathfrak{T})}{\partial \mathfrak{X}}\frac{\partial \mathfrak{w}(\mathfrak{X},\mathfrak{Y},\mathfrak{Z},\mathfrak{T})}{\partial \mathfrak{Y}}, \tag{6c}$$

$$\mathfrak{E}_{\mathfrak{X}\mathfrak{Z}} = \frac{1}{2}\left(\frac{\partial \mathfrak{w}(\mathfrak{X},\mathfrak{Y},\mathfrak{Z},\mathfrak{T})}{\partial \mathfrak{X}} + \frac{\partial \mathfrak{u}(\mathfrak{X},\mathfrak{Y},\mathfrak{Z},\mathfrak{T})}{\partial \mathfrak{Z}}\right), \tag{6d}$$

$$\mathfrak{E}_{\mathfrak{Y}\mathfrak{Z}} = \frac{1}{2}\left(\frac{\partial \mathfrak{w}(\mathfrak{X},\mathfrak{Y},\mathfrak{Z},\mathfrak{T})}{\partial \mathfrak{Y}} + \frac{\partial \mathfrak{v}(\mathfrak{X},\mathfrak{Y},\mathfrak{Z},\mathfrak{T})}{\partial \mathfrak{Z}}\right). \tag{6e}$$

The constitutive relations [37] of the silicon solar cell is

$$\begin{Bmatrix} \mathbb{T}_{\mathfrak{X}\mathfrak{X}} \\ \mathbb{T}_{\mathfrak{Y}\mathfrak{Y}} \\ \mathbb{T}_{\mathfrak{Y}\mathfrak{Z}} \\ \mathbb{T}_{\mathfrak{X}\mathfrak{Z}} \\ \mathbb{T}_{\mathfrak{X}\mathfrak{Y}} \end{Bmatrix} = \begin{Bmatrix} \mathfrak{s}_{11} & \mathfrak{s}_{12} & 0 & 0 & 0 \\ \mathfrak{s}_{21} & \mathfrak{s}_{22} & 0 & 0 & 0 \\ 0 & 0 & \mathfrak{s}_{44} & 0 & 0 \\ 0 & 0 & 0 & \mathfrak{s}_{55} & 0 \\ 0 & 0 & 0 & 0 & \mathfrak{s}_{66} \end{Bmatrix} \begin{Bmatrix} \mathfrak{E}_{\mathfrak{X}\mathfrak{X}} \\ \mathfrak{E}_{\mathfrak{Y}\mathfrak{Y}} \\ 2\mathfrak{E}_{\mathfrak{Y}\mathfrak{Z}} \\ 2\mathfrak{E}_{\mathfrak{X}\mathfrak{Z}} \\ 2\mathfrak{E}_{\mathfrak{X}\mathfrak{Y}} \end{Bmatrix}. \tag{7}$$

where $\mathfrak{s}_{ij}$ is the silicon solar cell's stiffness coefficient, $\mathbb{T}_{\mathfrak{x}\mathfrak{x}}$ and $\mathbb{T}_{\mathfrak{y}\mathfrak{y}}$ are the normal stress factors, $\mathbb{T}_{\mathfrak{y}\mathfrak{Z}}$, $\mathbb{T}_{\mathfrak{x}\mathfrak{Z}}$ and $\mathbb{T}_{\mathfrak{x}\mathfrak{y}}$ are the shear stress factors, and there are

$$\mathfrak{s}_{11} = \frac{E_i}{1-\nu_i^2}, \mathfrak{s}_{12} = \mathfrak{s}_{21} = \frac{\nu_i E_i}{1-\nu_i^2}, \mathfrak{s}_{22} = \frac{E_i}{1-\nu_i^2}, \tag{8a}$$

$$\mathfrak{s}_{66} = \frac{E_i}{2(1+\nu_i)}, \mathfrak{s}_{44} = \frac{E_i}{2(1+\nu_i)}, \mathfrak{s}_{55} = \frac{E_i}{2(1+\nu_i)}, i = 1, \dots, 8. \tag{8b}$$

## 3. Modified couple stress formulation

The modified pair stress theory is introduced by adding the extra term to the classical strain energy. The strain energy of the plate is defined as follows using the modified couple stress theory [38]:

$$U = \int_V \begin{Bmatrix} \left(\mathbb{T}_{\mathfrak{x}\mathfrak{x}}\mathfrak{E}_{\mathfrak{x}\mathfrak{x}} + \mathbb{T}_{\mathfrak{y}\mathfrak{y}}\mathfrak{E}_{\mathfrak{y}\mathfrak{y}} + 2\mathbb{T}_{\mathfrak{x}\mathfrak{Z}}\mathfrak{E}_{\mathfrak{x}\mathfrak{Z}} + 2\mathbb{T}_{\mathfrak{x}\mathfrak{y}}\mathfrak{E}_{\mathfrak{x}\mathfrak{y}} + 2\mathbb{T}_{\mathfrak{y}\mathfrak{Z}}\mathfrak{E}_{\mathfrak{y}\mathfrak{Z}}\right) \\ + \left(\mathfrak{m}_{\mathfrak{x}\mathfrak{x}}\mathfrak{d}_{\mathfrak{x}\mathfrak{x}} + \mathfrak{m}_{\mathfrak{y}\mathfrak{y}}\mathfrak{d}_{\mathfrak{y}\mathfrak{y}} + \mathfrak{m}_{\mathfrak{Z}\mathfrak{Z}}\mathfrak{d}_{\mathfrak{Z}\mathfrak{Z}} + 2\mathfrak{m}_{\mathfrak{x}\mathfrak{y}}\mathfrak{d}_{\mathfrak{x}\mathfrak{y}} + 2\mathfrak{m}_{\mathfrak{y}\mathfrak{Z}}\mathfrak{d}_{\mathfrak{y}\mathfrak{Z}} + 2\mathfrak{m}_{\mathfrak{x}\mathfrak{Z}}\mathfrak{d}_{\mathfrak{x}\mathfrak{Z}}\right)\} dV \end{Bmatrix} \tag{9}$$

where:

$$\mathfrak{d}_{ij} = \frac{1}{2}(\theta_{i,j} + \theta_{j,i}), \tag{10a}$$

$$\theta_i = \frac{1}{2} e_{ijk}\mathfrak{u}_{k,j}. \tag{10b}$$

where the permutation symbol is $e_{ijk}$. Additionally, the non-classical stress term ($\mathfrak{m}_{ij}$) is given as:

$$\mathfrak{m}_{ij} = 2\mu l^2 \mathfrak{d}_{ij}, \tag{11}$$

where $l$ is the additional material length scale parameter crucial to the rotation gradient and $\mu$ is the shear modulus. Consequently:

$$\mu = \frac{E_i}{2(1+\nu_i)}, \tag{12}$$

Eq. (9), which also entails performing mathematical operations and the starting variation of the kinetic energy and the variation of the strain energy, provides the set of governing equations of motion. where $A$ represents the plate's area. The components that arise from applying $d\mathfrak{Z}$ on $\mathbb{T}_{ij}$ and $\mathfrak{m}_{ij}$ are defined as follows:

$$\begin{aligned} \int_{-\frac{h}{2}}^{\frac{h}{2}} d\mathfrak{Z} = \int_{-\frac{h}{2}}^{-\frac{h}{2}+h_1} d\mathfrak{Z} + \int_{-\frac{h}{2}+h_1}^{-\frac{h}{2}+h_1+h_2} d\mathfrak{Z} + \int_{-h_3-h_4}^{-h_4} d\mathfrak{Z} + \int_{-h_4}^{0} d\mathfrak{Z} + \int_{0}^{h_5} d\mathfrak{Z} + + \int_{h_5}^{h_5+h_6} d\mathfrak{Z} \\ + \int_{h_5+h_6}^{h_5+h_6+h_7} d\mathfrak{Z} + \int_{\frac{h}{2}-h_8}^{\frac{h}{2}} d\mathfrak{Z} \end{aligned} \tag{13a}$$

$$\{\mathbb{o}_{ij}, \mathbb{p}_{ij}, \mathbb{q}_{ij}, \mathbb{q}^*_{ij}, \mathbb{r}_{ij}\} = \int_{-\frac{h}{2}}^{\frac{h}{2}} \left(1, \mathfrak{Z}, \frac{h}{\pi} sin\left(\frac{\pi\mathfrak{Z}}{h}\right), \frac{\pi}{h} sin\left(\frac{\pi\mathfrak{Z}}{h}\right), cos\left(\frac{\pi\mathfrak{Z}}{h}\right)\right) \mathbb{T}_{ij} d\mathfrak{Z}, \tag{13b}$$

$$\{\mathbb{s}_{ij}, \mathbb{t}_{ij}, \mathbb{t}^*_{ij}, \mathbb{u}_{ij}\} = \int_{-\frac{h}{2}}^{\frac{h}{2}} \left(1, \frac{h}{\pi} sin\left(\frac{\pi \mathfrak{Z}}{h}\right), \frac{\pi}{h} sin\left(\frac{\pi \mathfrak{Z}}{h}\right), cos\left(\frac{\pi \mathfrak{Z}}{h}\right)\right) \mathfrak{m}_{ij} d\mathfrak{Z}. \tag{13c}$$

The strain energy has the following final variation form when the subsequent components from Eqs. (13b-c) are substituted:

$$\begin{aligned}\delta U = \delta U_1 + \delta U_2 = \iint \Bigg\{ \Bigg( \left(-\frac{\partial \mathbb{o}_{\mathfrak{x}\mathfrak{x}}}{\partial \mathfrak{x}} - \frac{\partial \mathbb{o}_{\mathfrak{x}\mathfrak{y}}}{\partial \mathfrak{y}}\right)\delta \mathfrak{u} + \left(-\frac{\partial \mathbb{o}_{\mathfrak{x}\mathfrak{y}}}{\partial \mathfrak{x}} - \frac{\partial \mathbb{o}_{\mathfrak{y}\mathfrak{y}}}{\partial \mathfrak{y}}\right)\delta \mathfrak{v} + \left(-\frac{\partial^2 \mathbb{p}_{\mathfrak{x}\mathfrak{x}}}{\partial \mathfrak{x}^2} + \frac{\partial^2 \mathbb{q}_{\mathfrak{x}\mathfrak{x}}}{\partial \mathfrak{x}^2} - \right. \\ 2\frac{\partial^2 \mathbb{p}_{\mathfrak{x}\mathfrak{y}}}{\partial \mathfrak{y}\partial \mathfrak{x}} + 2\frac{\partial^2 \mathbb{q}_{\mathfrak{x}\mathfrak{y}}}{\partial \mathfrak{y}\partial \mathfrak{x}} - \frac{\partial \mathbb{r}_{\mathfrak{x}\mathfrak{Z}}}{\partial \mathfrak{x}} - \frac{\partial^2 \mathbb{p}_{\mathfrak{y}\mathfrak{y}}}{\partial \mathfrak{y}^2} + \frac{\partial^2 \mathbb{q}_{\mathfrak{y}\mathfrak{y}}}{\partial \mathfrak{y}^2} - \frac{\partial \mathbb{r}_{\mathfrak{y}\mathfrak{Z}}}{\partial \mathfrak{y}} + \frac{\partial}{\partial \mathfrak{x}}\left(\mathbb{o}_{\mathfrak{x}\mathfrak{x}}\frac{\partial \mathfrak{w}}{\partial \mathfrak{x}}\right) + \frac{\partial}{\partial \mathfrak{y}}\left(\mathbb{o}_{\mathfrak{y}\mathfrak{y}}\frac{\partial \mathfrak{w}}{\partial \mathfrak{y}}\right) + \\ \left.\frac{\partial}{\partial \mathfrak{y}}\left(\mathbb{o}_{\mathfrak{x}\mathfrak{y}}\frac{\partial \mathfrak{w}}{\partial \mathfrak{x}}\right) + \frac{\partial}{\partial \mathfrak{x}}\left(\mathbb{o}_{\mathfrak{x}\mathfrak{y}}\frac{\partial \mathfrak{w}}{\partial \mathfrak{y}}\right)\right)\delta \mathfrak{w} + \left(\frac{\partial \mathbb{q}_{\mathfrak{x}\mathfrak{x}}}{\partial \mathfrak{x}} + \frac{\partial \mathbb{q}_{\mathfrak{x}\mathfrak{y}}}{\partial \mathfrak{y}} - \mathbb{r}_{\mathfrak{x}\mathfrak{Z}}\right)\delta \mathfrak{S}_{\mathfrak{x}} + \left(\frac{\partial \mathbb{q}_{\mathfrak{x}\mathfrak{y}}}{\partial \mathfrak{x}} + \frac{\partial \mathbb{q}_{\mathfrak{y}\mathfrak{y}}}{\partial \mathfrak{y}} - \mathbb{r}_{\mathfrak{y}\mathfrak{Z}}\right)\delta \mathfrak{S}_{\mathfrak{y}}\Bigg) + \\ \Bigg(\left(-\frac{\partial^2 \mathbb{s}_{\mathfrak{y}\mathfrak{Z}}}{2\partial \mathfrak{y}^2} - \frac{\partial^2 \mathbb{s}_{\mathfrak{x}\mathfrak{Z}}}{2\partial \mathfrak{y}\partial \mathfrak{x}}\right)\delta \mathfrak{u} + \left(\frac{\partial^2 \mathbb{s}_{\mathfrak{y}\mathfrak{Z}}}{2\partial \mathfrak{y}\partial \mathfrak{x}} + \frac{\partial^2 \mathbb{s}_{\mathfrak{x}\mathfrak{Z}}}{2\partial \mathfrak{x}^2}\right)\delta \mathfrak{v} + \left(-\frac{1}{2}\frac{\partial \mathbb{t}^*_{\mathfrak{x}\mathfrak{Z}}}{\partial \mathfrak{y}} + \frac{1}{2}\frac{\partial \mathbb{t}^*_{\mathfrak{y}\mathfrak{Z}}}{\partial \mathfrak{x}} - \frac{\partial^2 \mathbb{s}_{\mathfrak{y}\mathfrak{y}}}{\partial \mathfrak{y}\partial \mathfrak{x}} + \frac{\partial^2 \mathbb{s}_{\mathfrak{x}\mathfrak{y}}}{\partial \mathfrak{y}^2} + \right. \\ \frac{\partial^2 \mathbb{s}_{\mathfrak{x}\mathfrak{x}}}{\partial \mathfrak{y}\partial \mathfrak{x}} - \frac{\partial^2 \mathbb{s}_{\mathfrak{x}\mathfrak{y}}}{\partial \mathfrak{x}^2} + \frac{\partial^2 \mathbb{u}_{\mathfrak{y}\mathfrak{y}}}{2\partial \mathfrak{y}\partial \mathfrak{x}} - \frac{\partial^2 \mathbb{u}_{\mathfrak{x}\mathfrak{y}}}{2\partial \mathfrak{y}^2} + \frac{\partial^2 \mathbb{u}_{\mathfrak{x}\mathfrak{y}}}{2\partial \mathfrak{x}^2} - \frac{\partial^2 \mathbb{u}_{\mathfrak{x}\mathfrak{x}}}{2\partial \mathfrak{y}\partial \mathfrak{x}}\Big)\delta \mathfrak{w} + \left(\frac{1}{2}\frac{\partial^2 \mathbb{t}_{\mathfrak{x}\mathfrak{Z}}}{\partial \mathfrak{y}\partial \mathfrak{x}} + \frac{\partial \mathbb{u}_{\mathfrak{y}\mathfrak{y}}}{2\partial \mathfrak{y}} + \frac{\partial \mathbb{u}_{\mathfrak{x}\mathfrak{y}}}{2\partial \mathfrak{x}} - \frac{\partial \mathbb{u}_{\mathfrak{3}\mathfrak{3}}}{2\partial \mathfrak{y}} + \right. \\ \left.\left.\frac{\mathbb{t}^*_{\mathfrak{y}\mathfrak{Z}}}{2} + \frac{1}{2}\frac{\partial^2 \mathbb{t}_{\mathfrak{y}\mathfrak{Z}}}{\partial \mathfrak{y}^2}\right)\delta \mathfrak{S}_{\mathfrak{x}} + \left(-\frac{1}{2}\frac{\partial^2 \mathbb{t}_{\mathfrak{x}\mathfrak{Z}}}{\partial \mathfrak{x}^2} - \frac{\mathbb{t}^*_{\mathfrak{x}\mathfrak{Z}}}{2} - \frac{1}{2}\frac{\partial^2 \mathbb{t}_{\mathfrak{y}\mathfrak{Z}}}{\partial \mathfrak{y}\partial \mathfrak{x}} - \frac{\partial \mathbb{u}_{\mathfrak{x}\mathfrak{x}}}{2\partial \mathfrak{x}} - \frac{\partial \mathbb{u}_{\mathfrak{x}\mathfrak{y}}}{2\partial \mathfrak{y}} + \frac{\partial \mathbb{u}_{\mathfrak{3}\mathfrak{3}}}{2\partial \mathfrak{x}}\right)\delta \mathfrak{S}_{\mathfrak{y}}\Bigg)\Bigg\} dA,\end{aligned} \tag{14}$$

where $U_1$ and $U_2$ represent the classical and non-classical components of the strain energy, respectively. The variability in kinetic energy is expressed as follows:

$$\begin{aligned}\mu = \frac{E_i}{2(1+\nu_i)}, \delta T = \iint \Big\{ \Big(-\mathfrak{K}_0 \frac{\partial^2 \mathfrak{u}}{\partial \mathfrak{T}^2} + \mathfrak{K}_1 \frac{\partial^3 \mathfrak{w}}{\partial \mathfrak{x}\partial \mathfrak{T}^2} - \mathfrak{K}_3 \frac{\partial^3 \mathfrak{w}}{\partial \mathfrak{x}\partial \mathfrak{T}^2} + \mathfrak{K}_3 \frac{\partial^2 \mathfrak{S}_{\mathfrak{x}}}{\partial \mathfrak{T}^2}\Big)\delta \mathfrak{u} + \Big(-\mathfrak{K}_0 \frac{\partial^2 \mathfrak{v}}{\partial \mathfrak{T}^2} + \\ \mathfrak{K}_1 \frac{\partial^3 \mathfrak{w}}{\partial \mathfrak{y}\partial \mathfrak{T}^2} - \mathfrak{K}_3 \frac{\partial^3 \mathfrak{w}}{\partial \mathfrak{y}\partial \mathfrak{T}^2} + \mathfrak{K}_3 \frac{\partial^2}{\partial \mathfrak{T}^2}\mathfrak{S}_{\mathfrak{y}}\Big)\delta \mathfrak{v} + \Big(-\mathfrak{K}_1 \frac{\partial^3 \mathfrak{u}}{\partial \mathfrak{x}\partial \mathfrak{T}^2} + \mathfrak{K}_3 \frac{\partial^3 \mathfrak{u}}{\partial \mathfrak{x}\partial \mathfrak{T}^2} + \mathfrak{K}_2 \frac{\partial^4 \mathfrak{w}}{\partial \mathfrak{x}^2\partial \mathfrak{T}^2} - \\ 2\mathfrak{K}_5 \frac{\partial^4 \mathfrak{w}}{\partial \mathfrak{x}^2\partial \mathfrak{T}^2} + \mathfrak{K}_5 \frac{\partial^3 \mathfrak{S}_{\mathfrak{x}}}{\partial \mathfrak{x}\partial \mathfrak{T}^2} + \mathfrak{K}_4 \frac{\partial^4 \mathfrak{w}}{\partial \mathfrak{x}^2\partial \mathfrak{T}^2} - \mathfrak{K}_4 \frac{\partial^3 \mathfrak{S}_{\mathfrak{x}}}{\partial \mathfrak{x}\partial \mathfrak{T}^2} - \mathfrak{K}_1 \frac{\partial^3 \mathfrak{v}}{\partial \mathfrak{y}\partial \mathfrak{T}^2} + \mathfrak{K}_3 \frac{\partial^3 \mathfrak{v}}{\partial \mathfrak{y}\partial \mathfrak{T}^2} + \mathfrak{K}_2 \frac{\partial^4 \mathfrak{w}}{\partial \mathfrak{y}^2\partial \mathfrak{T}^2} - \\ 2\mathfrak{K}_5 \frac{\partial^4 \mathfrak{w}}{\partial \mathfrak{y}^2\partial \mathfrak{T}^2} + \mathfrak{K}_5 \frac{\partial^3 \mathfrak{S}_{\mathfrak{y}}}{\partial \mathfrak{y}\partial \mathfrak{T}^2} + \mathfrak{K}_4 \frac{\partial^4 \mathfrak{w}}{\partial \mathfrak{y}^2\partial \mathfrak{T}^2} - \mathfrak{K}_4 \frac{\partial^3 \mathfrak{S}_{\mathfrak{y}}}{\partial \mathfrak{y}\partial \mathfrak{T}^2} - \mathfrak{K}_0 \frac{\partial^2 \mathfrak{w}}{\partial \mathfrak{T}^2}\Big)\delta \mathfrak{w} + \Big(\mathfrak{K}_3 \frac{\partial^2 \mathfrak{u}}{\partial \mathfrak{T}^2} - \mathfrak{K}_5 \frac{\partial^3 \mathfrak{w}}{\partial \mathfrak{x}\partial \mathfrak{T}^2} + \\ \mathfrak{K}_4 \frac{\partial^3 \mathfrak{w}}{\partial \mathfrak{x}\partial \mathfrak{T}^2} - \mathfrak{K}_4 \frac{\partial^2 \mathfrak{S}_{\mathfrak{x}}}{\partial \mathfrak{T}^2}\Big)\delta \mathfrak{S}_{\mathfrak{x}} + \Big(\mathfrak{K}_3 \frac{\partial^2 \mathfrak{v}}{\partial \mathfrak{T}^2} - \mathfrak{K}_5 \frac{\partial^3 \mathfrak{w}}{\partial \mathfrak{y}\partial \mathfrak{T}^2} + \mathfrak{K}_4 \frac{\partial^3 \mathfrak{w}}{\partial \mathfrak{y}\partial \mathfrak{T}^2} - \mathfrak{K}_4 \frac{\partial^2 \mathfrak{S}_{\mathfrak{y}}}{\partial \mathfrak{T}^2}\Big)\delta \mathfrak{S}_{\mathfrak{y}}\Big\} dA\end{aligned} \tag{15}$$

And the following is the definition of the integration constants:

$$\begin{aligned}\int_{-\frac{h}{2}}^{\frac{h}{2}} d\mathfrak{Z} = \int_{-\frac{h}{2}}^{-\frac{h}{2}+h_1} d\mathfrak{Z} + \int_{-\frac{h}{2}+h_1}^{-\frac{h}{2}+h_1+h_2} d\mathfrak{Z} + \int_{-h_3-h_4}^{-h_4} d\mathfrak{Z} + \int_{-h_4}^{0} d\mathfrak{Z} + \int_{0}^{h_5} d\mathfrak{Z} + + \int_{h_5}^{h_5+h_6} d\mathfrak{Z} + \\ \int_{h_5+h_6}^{h_5+h_6+h_7} d\mathfrak{Z} + \int_{\frac{h}{2}-h_8}^{\frac{h}{2}} d\mathfrak{Z}.\end{aligned} \tag{16a}$$

$$\{\mathfrak{K}_0, \mathfrak{K}_1, \mathfrak{K}_2, \mathfrak{K}_3, \mathfrak{K}_4, \mathfrak{K}_5\} = \int_{-\frac{h}{2}}^{\frac{h}{2}} \rho\left\{1, \mathfrak{Z}, \mathfrak{Z}^2, \frac{h}{\pi} sin(\frac{\pi \mathfrak{Z}}{h}), \frac{h^2}{\pi^2} sin2(\frac{\pi \mathfrak{Z}}{h}), \frac{h\mathfrak{Z}}{\pi} sin(\frac{\pi \mathfrak{Z}}{h})\right\} d\mathfrak{Z}, \tag{16b}$$

Additionally, the Winkler-Pasternak Foundation's efforts might be described as

$$\delta W = \iint \left\{-K_w \mathfrak{w} + K_p \left(\frac{\partial^2 \mathfrak{w}}{\partial \mathfrak{x}^2} + \frac{\partial^2 \mathfrak{w}}{\partial \mathfrak{y}^2}\right)\right\} dA \tag{17}$$

Hamilton's principle yields five equations of motion that control the issue, which are as follows:

$$-\mathfrak{K}_0\frac{\partial^2 \mathfrak{u}}{\partial \mathfrak{T}^2}+\mathfrak{K}_1\frac{\partial^3 \mathfrak{w}}{\partial \mathfrak{x}\partial \mathfrak{T}^2}-\mathfrak{K}_3\frac{\partial^3 \mathfrak{w}}{\partial \mathfrak{x}\partial \mathfrak{T}^2}+\mathfrak{K}_3\frac{\partial^2 \mathfrak{S}_\mathfrak{x}}{\partial \mathfrak{T}^2}+\frac{\partial^2 \mathfrak{s}_{\mathfrak{y}3}}{2\partial \mathfrak{y}^2}+\frac{\partial^2 \mathfrak{s}_{\mathfrak{x}3}}{2\partial \mathfrak{y}\partial \mathfrak{x}}+\frac{\partial \mathbb{o}_{\mathfrak{x}\mathfrak{x}}}{\partial \mathfrak{x}}+\frac{\partial \mathbb{o}_{\mathfrak{x}\mathfrak{y}}}{\partial \mathfrak{y}}=0, \tag{18a}$$

$$\mathfrak{K}_3\frac{\partial^2 \mathfrak{S}_\mathfrak{y}}{\partial \mathfrak{T}^2}+\mathfrak{K}_1\frac{\partial^3 \mathfrak{w}}{\partial \mathfrak{y}\partial \mathfrak{T}^2}-\mathfrak{K}_0\frac{\partial^2 \mathfrak{v}}{\partial \mathfrak{T}^2}-\mathfrak{K}_3\frac{\partial^3 \mathfrak{w}}{\partial \mathfrak{y}\partial \mathfrak{T}^2}-\frac{\partial^2 \mathfrak{s}_{\mathfrak{y}3}}{2\partial \mathfrak{y}\partial \mathfrak{x}}-\frac{\partial^2 \mathfrak{s}_{\mathfrak{x}3}}{2\partial \mathfrak{x}^2}+\frac{\partial \mathbb{o}_{\mathfrak{x}\mathfrak{y}}}{\partial \mathfrak{x}}+\frac{\partial \mathbb{o}_{\mathfrak{y}\mathfrak{y}}}{\partial \mathfrak{y}}=0, \tag{18b}$$

$$\begin{gathered}\mathfrak{K}_3\frac{\partial^3 \mathfrak{u}}{\partial \mathfrak{x}\partial \mathfrak{T}^2}-\mathfrak{K}_1\frac{\partial^3 \mathfrak{u}}{\partial \mathfrak{x}\partial \mathfrak{T}^2}+\mathfrak{K}_3\frac{\partial^3 \mathfrak{v}}{\partial \mathfrak{y}\partial \mathfrak{T}^2}-\mathfrak{K}_1\frac{\partial^3 \mathfrak{v}}{\partial \mathfrak{y}\partial \mathfrak{T}^2}-2\mathfrak{K}_5\frac{\partial^4 \mathfrak{w}}{\partial \mathfrak{x}^2\partial \mathfrak{T}^2}-\mathfrak{K}_0\frac{\partial^2 \mathfrak{w}}{\partial \mathfrak{T}^2}+\mathfrak{K}_4\frac{\partial^4 \mathfrak{w}}{\partial \mathfrak{y}^2\partial \mathfrak{T}^2}+\\ \mathfrak{K}_2\frac{\partial^4 \mathfrak{w}}{\partial \mathfrak{y}^2\partial \mathfrak{T}^2}-2\mathfrak{K}_5\frac{\partial^4 \mathfrak{w}}{\partial \mathfrak{y}^2\partial \mathfrak{T}^2}+\mathfrak{K}_2\frac{\partial^4 \mathfrak{w}}{\partial \mathfrak{x}^2\partial \mathfrak{T}^2}+\mathfrak{K}_4\frac{\partial^4 \mathfrak{w}}{\partial \mathfrak{x}^2\partial \mathfrak{T}^2}-\frac{\partial^2 \mathbb{q}_{\mathfrak{x}\mathfrak{x}}}{\partial \mathfrak{x}^2}-\frac{2\partial^2 \mathbb{q}_{\mathfrak{x}\mathfrak{y}}}{\partial \mathfrak{y}\partial \mathfrak{x}}-\frac{\partial^2 \mathbb{q}_{\mathfrak{y}\mathfrak{y}}}{\partial \mathfrak{y}^2}+\mathfrak{K}_5\frac{\partial^3 \mathfrak{S}_\mathfrak{y}}{\partial \mathfrak{y}\partial \mathfrak{T}^2}-\\ \mathfrak{K}_4\frac{\partial^3 \mathfrak{S}_\mathfrak{y}}{\partial \mathfrak{y}\partial \mathfrak{T}^2}-\mathfrak{K}_4\frac{\partial^3 \mathfrak{S}_\mathfrak{x}}{\partial \mathfrak{x}\partial \mathfrak{T}^2}+\mathfrak{K}_5\frac{\partial^3 \mathfrak{S}_\mathfrak{x}}{\partial \mathfrak{x}\partial \mathfrak{T}^2}+\frac{\partial}{\partial \mathfrak{x}}\left(\mathbb{o}_{\mathfrak{x}\mathfrak{x}}\frac{\partial \mathfrak{w}}{\partial \mathfrak{x}}\right)+\frac{\partial}{\partial \mathfrak{y}}\left(\mathbb{o}_{\mathfrak{y}\mathfrak{y}}\frac{\partial \mathfrak{w}}{\partial \mathfrak{y}}\right)+\frac{\partial}{\partial \mathfrak{y}}\left(\mathbb{o}_{\mathfrak{x}\mathfrak{y}}\frac{\partial \mathfrak{w}}{\partial \mathfrak{x}}\right)+\\ \frac{\partial}{\partial \mathfrak{x}}\left(\mathbb{o}_{\mathfrak{x}\mathfrak{y}}\frac{\partial \mathfrak{w}}{\partial \mathfrak{y}}\right)+\frac{\partial^2 \mathbb{p}_{\mathfrak{y}\mathfrak{y}}}{\partial \mathfrak{y}^2}+\frac{2\partial^2 \mathbb{p}_{\mathfrak{x}\mathfrak{y}}}{\partial \mathfrak{y}\partial \mathfrak{x}}+\frac{\partial^2 \mathbb{p}_{\mathfrak{x}\mathfrak{x}}}{\partial \mathfrak{x}^2}+\frac{\partial \mathbb{r}_{\mathfrak{y}3}}{\partial \mathfrak{y}}+\frac{\partial \mathbb{r}_{\mathfrak{x}3}}{\partial \mathfrak{x}}+\frac{\partial \mathbb{t}^*_{\mathfrak{x}3}}{2\partial \mathfrak{y}}-\frac{\partial \mathbb{t}^*_{\mathfrak{y}3}}{2\partial \mathfrak{x}}-\frac{\partial^2 \mathbb{u}_{\mathfrak{y}\mathfrak{y}}}{2\partial \mathfrak{y}\partial \mathfrak{x}}-\frac{\partial^2 \mathbb{u}_{\mathfrak{x}\mathfrak{y}}}{2\partial \mathfrak{x}^2}+\\ \frac{\partial^2 \mathbb{u}_{\mathfrak{x}\mathfrak{x}}}{2\partial \mathfrak{y}\partial \mathfrak{x}}+\frac{\partial^2 \mathbb{u}_{\mathfrak{x}\mathfrak{y}}}{2\partial \mathfrak{y}^2}-\frac{\partial^2 \mathbb{s}_{\mathfrak{x}\mathfrak{x}}}{\partial \mathfrak{y}\partial \mathfrak{x}}+\frac{\partial^2 \mathbb{s}_{\mathfrak{x}\mathfrak{y}}}{\partial \mathfrak{x}^2}+\frac{\partial^2 \mathbb{s}_{\mathfrak{y}\mathfrak{y}}}{\partial \mathfrak{y}\partial \mathfrak{x}}-\frac{\partial^2 \mathbb{s}_{\mathfrak{x}\mathfrak{y}}}{\partial \mathfrak{y}^2}-K_w\mathfrak{w}+K_p\left(\frac{\partial^2 \mathfrak{w}}{\partial \mathfrak{x}^2}+\frac{\partial^2 \mathfrak{w}}{\partial \mathfrak{y}^2}\right)=0,\end{gathered} \tag{18c}$$

$$\begin{gathered}\mathfrak{K}_3\frac{\partial^2 \mathfrak{u}}{\partial \mathfrak{T}^2}-\mathfrak{K}_5\frac{\partial^3 \mathfrak{w}}{\partial \mathfrak{x}\partial \mathfrak{T}^2}-\mathfrak{K}_4\frac{\partial^2 \mathfrak{S}_\mathfrak{x}}{\partial \mathfrak{T}^2}+\mathfrak{K}_4\frac{\partial^3 \mathfrak{w}}{\partial \mathfrak{x}\partial \mathfrak{T}^2}-\frac{\partial^2 \mathbb{t}_{\mathfrak{y}3}}{2\partial \mathfrak{y}^2}-\frac{\partial^2 \mathbb{t}_{\mathfrak{x}3}}{2\partial \mathfrak{y}\partial \mathfrak{x}}-\frac{\mathbb{t}^*_{\mathfrak{y}3}}{2}-\frac{\partial \mathbb{u}_{\mathfrak{x}\mathfrak{y}}}{2\partial \mathfrak{x}}+\frac{\partial \mathbb{u}_{3\mathfrak{3}}}{2\partial \mathfrak{y}}-\frac{\partial \mathbb{u}_{\mathfrak{y}\mathfrak{y}}}{2\partial \mathfrak{y}}-\\ \frac{\partial \mathbb{q}_{\mathfrak{x}\mathfrak{x}}}{\partial \mathfrak{x}}-\frac{\partial \mathbb{q}_{\mathfrak{x}\mathfrak{y}}}{\partial \mathfrak{y}}+\mathbb{r}_{\mathfrak{x}3}=0,\end{gathered} \tag{18d}$$

$$\begin{gathered}-\mathfrak{K}_4\frac{\partial^2 \mathfrak{S}_\mathfrak{y}}{\partial \mathfrak{T}^2}+\mathfrak{K}_3\frac{\partial^2 \mathfrak{v}}{\partial \mathfrak{T}^2}+\mathfrak{K}_4\frac{\partial^3 \mathfrak{w}}{\partial \mathfrak{y}\partial \mathfrak{T}^2}-\mathfrak{K}_5\frac{\partial^3 \mathfrak{w}}{\partial \mathfrak{y}\partial \mathfrak{T}^2}+\frac{\partial^2 \mathbb{t}_{\mathfrak{x}3}}{2\partial \mathfrak{x}^2}+\frac{\partial^2 \mathbb{t}_{\mathfrak{y}3}}{2\partial \mathfrak{y}\partial \mathfrak{x}}+\frac{\mathbb{t}^*_{\mathfrak{x}3}}{2}+\frac{\partial \mathbb{u}_{\mathfrak{x}\mathfrak{y}}}{2\partial \mathfrak{y}}-\frac{\partial \mathbb{u}_{3\mathfrak{3}}}{2\partial \mathfrak{x}}+\frac{\partial \mathbb{u}_{\mathfrak{x}\mathfrak{x}}}{2\partial \mathfrak{x}}-\\ \frac{\partial \mathbb{q}_{\mathfrak{x}\mathfrak{y}}}{\partial \mathfrak{x}}-\frac{\partial \mathbb{q}_{\mathfrak{y}\mathfrak{y}}}{\partial \mathfrak{y}}+\mathbb{r}_{\mathfrak{y}3}=0,\end{gathered} \tag{18e}$$

## 4. Solution method

We make the following assumption:

$$\begin{aligned}\mathfrak{u}_0&=\bar{\mathfrak{u}}_0 e^{i(K_X\mathfrak{x}+K_Y\mathfrak{y}-\omega\mathfrak{T})},\\ \mathfrak{v}_0&=\bar{\mathfrak{v}}_0 e^{i(K_X\mathfrak{x}+K_Y\mathfrak{y}-\omega\mathfrak{T})},\\ \mathfrak{w}_0&=\bar{\mathfrak{w}}_0 e^{i(K_X\mathfrak{x}+K_Y\mathfrak{y}-\omega\mathfrak{T})},\\ \mathfrak{S}_\mathfrak{x}&=\bar{\mathfrak{S}}_\mathfrak{x} e^{i(K_X\mathfrak{x}+K_Y\mathfrak{y}-\omega\mathfrak{T})},\\ \mathfrak{S}_\mathfrak{y}&=\bar{\mathfrak{S}}_\mathfrak{y} e^{i(K_X\mathfrak{x}+K_Y\mathfrak{y}-\omega\mathfrak{T})}.\end{aligned} \tag{19}$$

where $\omega$ denotes the wave frequency, $K_X$, and $K_Y$ are specified to identify the wave numbers, and $\bar{\mathfrak{u}}_0$, $\bar{\mathfrak{v}}_0$, $\bar{\mathfrak{w}}_0$, $\bar{\mathfrak{S}}_\mathfrak{x}$, and $\bar{\mathfrak{S}}_\mathfrak{y}$ introduce the wave amplitudes. Eqs. (13a-c), (16a-b), and (19) are substituted into Eqs. (18a-e) to yield the eigenvalue equation, after which the nonlinear components and external load are removed.

$$([\mathbb{k}_L]+[\mathbb{k}_{NL}]-\omega^2[\mathfrak{m}])\{\Delta\}=0 \tag{20}$$

where $\{\Delta\}=\{\bar{\mathfrak{u}}_0 \quad \bar{\mathfrak{v}}_0 \quad \bar{\mathfrak{w}}_0 \quad \bar{\mathfrak{S}}_\mathfrak{x} \quad \bar{\mathfrak{S}}_\mathfrak{y}\}^T$, where $[\mathbb{k}_L]$ and $[\mathfrak{m}]$ describe the linear stiffness matrix,

nonlinear stiffness matrix, and mass matrix, respectively. Additionally, Eq. (21) may be used to derive the phase velocity.

$$Phase\ velocity = \frac{\omega}{K_X} \tag{21}$$

Also, dimensionless quantities are defined by

$$K_W^* = \frac{K_w a^4}{EI}, K_P^* = \frac{K_p a^2}{EI}. \tag{22}$$

## 5. Combining DNN with GA as a bio-inspired optimization method to forecast the propagation of nonlinear waves in silicon solar cells

The demand for efficient, renewable energy solutions is on the rise and this has led to the application of better-performing photovoltaic systems, particularly silicon solar cells, as a main focus of study. Since silicon is still the leading material in solar cell technology, the understanding of the behavior of nonlinear wave propagation in silicon cells is very fundamental for making them more efficient and also improving their overall functions. In fact, there are many nonlinear wave effects that take place in solar cells and these are based on the complex light interactions and the imperfections in the materials used and the performance of the solar cells depends greatly on these phenomena. Thus, the prediction and the calibration of these behaviors are very much in the forefront of efficient solar energy technologies. There are traditional methods of simulating nonlinear wave propagation, but they are of high value, and at the same time, they suffer from very high complexity and computational costs. However, in the recent years, the application of living organisms' traits in the development of the GA combined with the use of modern-day neural networks has been a great breakthrough in tackling the problems of complexity and computational costs. DNN, which are a type of machine learning model, are those that can cope with the complex, nonlinear problems very well since they can identify very detailed patterns in the data. Unlike the DNNs, Genetic Algorithms are straightforward and, therefore, do not charge by the principles of natural selection and evolution and provide a strong optimization framework that can accommodate various and high-dimensional search spaces. The hybrid bio-inspired optimization technique made up of DNN and GA is a great tool for predicting the spread of nonlinear waves in silicon solar cells. The DNN part is very good at figuring out and anticipating the intricate connections between the many input variables (like the properties of the materials, the intensity of the light, and the configurations of the structure) and the resulting behavior (characteristics of wave propagation). On the other hand, the GA is used to fine-tune the DNN parameters, thus making it sure that the model is perfectly adjusted for accuracy and predictive trustworthiness. DNN and GA together offer a solution to the inverse problems of nonlinear wave propagation that is particularly advantageous. The use of GA in looking for the best among the neural network architecture and training parameters means that the model can have a greater level of generalization and accuracy. Furthermore, the GA can help in pointing out the variables that mainly affect silicon wave propagation and that may not be easy to distinguish using the usual analytical techniques. This combined method is not only fast in terms of computation but also versatile, thus providing a loose framework for predicting wave behaviors under different environmental and material conditions. Using DNN and GA for predicting nonlinear wave propagation is a new and still unexplored method of research, which can significantly facilitate the

design and optimization of silicon solar cells. The combination of these bio-inspired techniques will allow the researchers to deepen the knowledge of wave dynamics in solar cells and also to get better predictive models which are necessary for high-efficiency solar energy systems designing. This soution supports the contemporary movement towards interdisciplinary collaborations that utilize AI and optimization methods in combination to solve complicated engineering issues. The suggested approach would be one step for others to follow in the path of solar cell technology innovations, and consequently, lead to getting electricity more efficiently and to having less environmentally harmful solar energy production in the world.

### 5.1 Implementation details and Hyperparameters

The DNN-GA model's training dataset was made using the numerical solution of the governing equations (Eqs. 20a-e) through the RK4 method explained in Section 4.1. The fixation of 15,000 periodic samples was done by altering the principal input factors: GPL weight fraction (0-0.4), length scale parameter ($h/20$ to $h/8$), wavenumber ($0 - 10^4$), and GPL distribution pattern (X, O, UD). Then each sample matched these variables to their respective nonlinear wave response outputs: displacements and phase velocity at the center of the plate. The DNN was composed of an input layer (6 neurons), four hidden layers (64 neurons each with ReLU activation), and an output layer (3 neurons with linear activation). The GA was applied to optimize the network's weights and biases with a population size of 50 for the span of 100 generations. The tournament selection (size 3) was used for selection, the single-point crossover (rate 0.8) for crossover, and the random Gaussian perturbation (rate 0.1, σ=0.05) for mutation. The Mean Squared Error (MSE) on the training set was used as the fitness function in the inverse form. The model's accuracy was checked by the coefficient of determination ($R^2$) and MSE on a separate test set (15% of the total data), while the training process was supervised by loss curves to preclude overfitting. The DNN's predictions take on the role of a fast surrogate for the resource-demanding numerical integration, directly approximating the functional relationship $f: (g_{GPL}, l, K_X, \dots) \rightarrow (\mathfrak{u}_0, \mathfrak{w}_0, Phase\ Velocity)$ that the underlying physics in Eqs. 18-20 define.

## 6. Result and discussion

### 6.1 Validation

Table 3 indicates the dimensionless fundamental natural frequencies of different plates, on the other hand, the epoxy and the graphene-reinforced materials (GPL-UD, GPL-O, and GPL-X) are the ones used for comparison. The table presents two different sets of values: one from the reference study (Ref. [39]) and the other from the current study. The first study shows the frequency for pure epoxy to be 0.0584, while the current study records it as 0.0585, which is slightly higher. The increase in the natural frequency in the present study is very small but significant and may be indicative of not only slightly differing material properties but also variations in analysis techniques. Natural frequencies of graphene-reinforced plates are noticeably higher than those of pure epoxy. The GPL-UD plate has the highest fundamental frequency of 0.1216 (Ref. [39]) and 0.1218 (present study) in the case of both studies. The GPL-O and GPL-X plates show somewhat lower values, with frequencies of 0.1020 and 0.1378 for the reference and 0.1022 and 0.1379 for the present study. The values point towards the conclusion that graphene reinforcement results in higher natural frequencies, especially for GPL-UD and GPL-X

Table 3. Dimensionless fundamental natural frequencies of plates

| | Pure epoxy | GPL-UD | GPL-O | GPL-X |
|---|---|---|---|---|
| Ref. [39] | 0.0584 | 0.1216 | 0.1020 | 0.1378 |
| Present study | 0.0585 | 0.1218 | 0.1022 | 0.1379 |

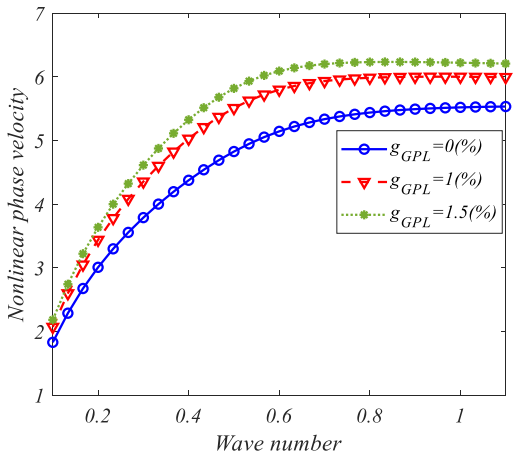


Figure 2. The impact of GPL weight percentage and wave number on the structure's nonlinear phase velocity

configurations thus indicating better stiffness and dynamic response in the composite materials based on graphene. The current study confirms previous research results and at the same time points out the significant role of graphene reinforcement in changing composite plates' dynamic characteristics.

## 6.2 Parametric study

Fig. 2 shows how the weight fraction of graphene platelets affects the nonlinear phase velocity versus wave number. Different weight fractions of graphene platelets, namely 0%, 1%, and 1.5%, are represented by the different curves. The horizontal axis indicates the wave number, and the vertical axis indicates the nonlinear phase velocity. It can be seen that the weight fraction of graphene platelets is an important factor for the nonlinear phase velocity since even a small amount (1%) of graphene itself leads to a considerable increase of the phase velocity. This not only confirms the notion that the increase in graphene content ultimately improves the wave propagation, but also hints at the fact that the so-called "stiffness" along with the better mechanical properties delivered by the graphene reinforcement are major factors for the improvement. Thus, the nonlinear phase velocity rises quite rapidly at lower wave numbers, but the rise peaks and alone rate of growth decreases as the wave number increases. The observed trend illustrates how vital the weight fraction of graphene platelets is in tuning the dynamic response of the solar cell plates, thus showing that even the smallest amounts of reinforcement content may play an important role in the oscillation of the wave throughout the advanced composite systems.

Fig. 3 illustrates how the ratio of length scale parameters influences the nonlinear phase velocity as a function of the wave number. The different lines correspond to the ratios of length

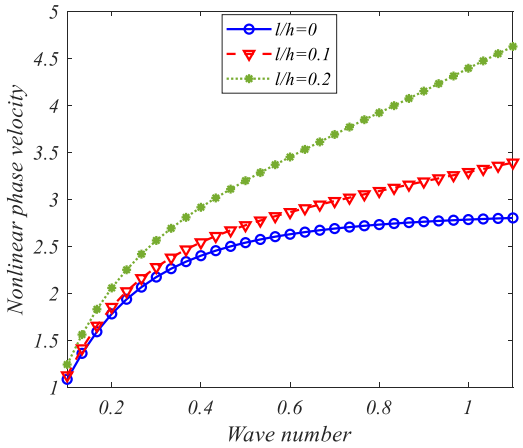


Figure 3. The impact of $l/h$ parameters and wave number on the structure's nonlinear phase velocity

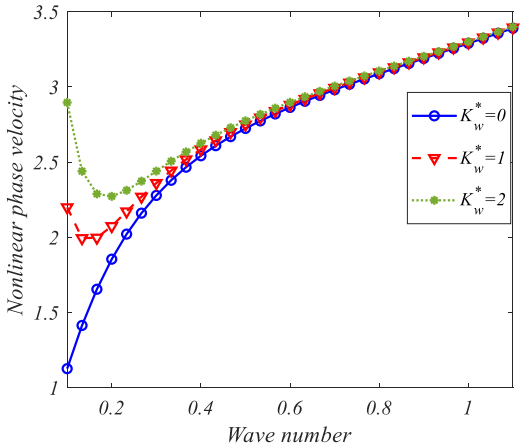


Figure 4. The impact of $K_W^*$ parameter and wave number on the structure's nonlinear phase velocity

scale parameters of 0, 0.1, and 0.2, respectively. The x-axis represents the wave number and the y-axis shows the nonlinear phase velocity. The plot clearly indicates that the higher the length scale parameter ratio the more the nonlinear phase velocity is increased, especially at higher wave numbers. This behavior is representative of strong size-dependent effects, where the microstructural length scale becomes more and more important in determining the whole wave dynamics. Moreover, the difference between the curves increases as the wave number increases, which indicates that it is necessary to consider size effects in the modeling of micro-scale solar cell structures. Thus, the figure demonstrates the significance of the length scale parameter ratio in not only making the non-classical mechanical behavior of graphene-reinforced composites for solar cells more apparent but also in optimizing their wave propagation properties.

Fig. 4 underscores the importance of the dimensionless Winkler coefficient in modifying the nonlinear phase velocity depending on the wave number. The Winker coefficient is being altered from 0 to 1 and 2, which is indicated by the three different curves. The horizontal axis signifies the wave number, while the vertical axis denotes the nonlinear phase velocity. Examining the curves

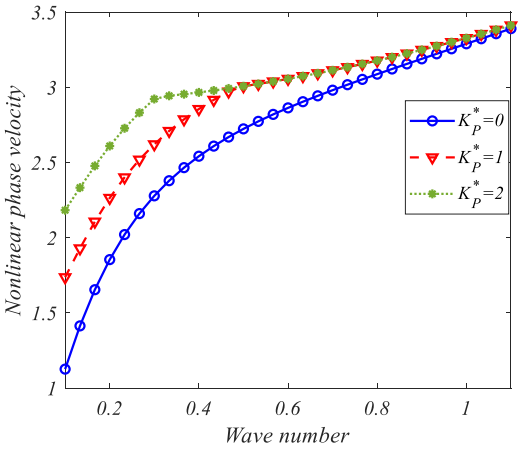


Figure 5. The impact of $K_P^*$ parameter and wave number on the structure's nonlinear phase velocity

reveals how a rise in the dimensionless Winkler coefficient causes a slight rise in the nonlinear phase velocity, especially at low wave numbers. The influence reduces as the wave number rises, and the curves meet again at the highest wave numbers. These results indicate that the Winkler foundation, which simulates the medium's elastic response, is more significant in the lower wave number zone. The findings indicate that adjusting the dimensionless Winkler coefficient is a reliable method for regulating the initial dynamic response of the composite system, thus facilitating the development of solar cells with specific vibrational properties for better performance and stability through conferring an indirect role of the structure in the selection of the working wavelength range.

Fig. 5 shows how the dimensionless Pasternak coefficient affects the nonlinear phase velocity for different sums of wave numbers. The coefficient changes are from 0, 1, and 2, respectively, for the three curves. The wave number is shown on the horizontal axis, whereas the nonlinear phase velocity is depicted on the vertical axis. It can be seen that the rise in the dimensionless Pasternak coefficient, which is the shear interaction estimation of the elastic foundation, causes the nonlinear phase velocity increase at all wave numbers, although to a lesser degree. The influence is most pronounced at the lowest wave numbers and then gradually lessens with an increase in wave number, yet a difference between the curves that cannot be ignored is still present. Thus, it can be concluded that the use of shear interactions through the Pasternak foundation is essential for accurately portraying the wave propagation characteristics in graphene-reinforced composites. The results support the assumption that both Winkler and Pasternak coefficients need to be taken into account when modeling the foundation effects to avoid weak and unrealistic forecasts for the dynamic behavior of advanced solar cell plates.

Fig. 6 elaborates on the non-linear phase velocity's dependency on the dimensionless Winkler coefficient and different dimensionless Pasternak coefficients. The dimensionless Winkler coefficient takes the position of the horizontal axis, whereas the non-linear phase velocity is plotted on the vertical axis. For the dimensionless Pasternak coefficient values of 0, 0.5, and 1, three distinct curves are displayed. The outcome illustrates that with the dimensionless Winkler coefficient growing, the nonlinear phase velocity follows in a nonlinear way. In addition, at a fixed Winkler coefficient value, the Pasternak coefficient increment results in a higher nonlinear phase

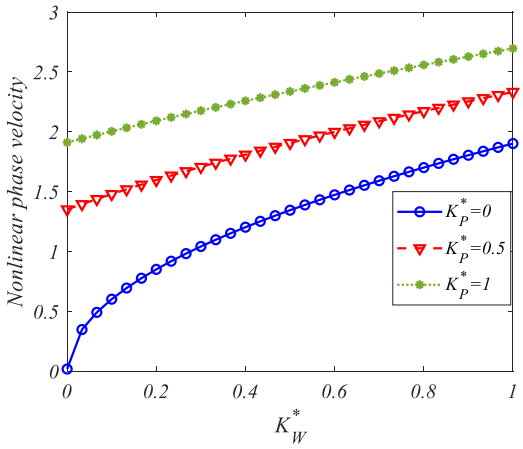


Figure 6. The impact of $K_P^*$ and $K_P^*$ parameters on the structure's nonlinear phase velocity

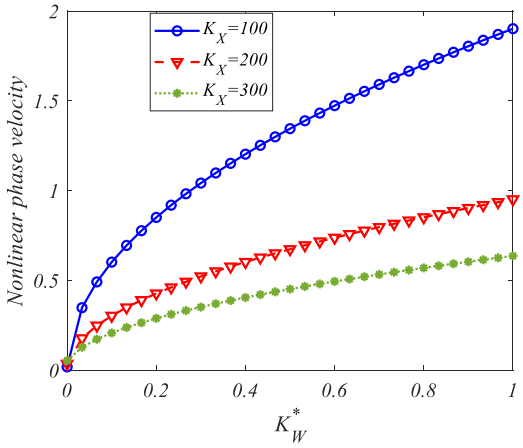


Figure 7. The impact of $K_W^*$ parameter and wave number on the structure's nonlinear phase velocity

velocity. This means that the magnitudes of both the Winkler and Pasternak foundation parameters are together uplifting the dynamical wave propagation characteristics of the composite system. Moreover, the non-linear phase velocity's sensitivity to these foundation parameters points out their significance in the structural design and vibration control of graphene-reinforced solar cell plates. The findings suggest that the coefficients must be optimized in a combined manner to get the dynamic responses that are appropriate for next-generation micro-structured solar cell applications.

Fig. 7 examines how a stiffness-related parameter (represented by three different values) affects the nonlinear phase velocity versus the dimensionless Winkler coefficient. The horizontal axis indicates the dimensionless Winkler coefficient, and the nonlinear phase velocity is represented on the vertical axis. The transition lines are associated with three ascending stiffness-related parameter values indicated as 100, 200, and 300, respectively. It is clearly seen that the nonlinearity phase velocity is inversely proportional to the stiffness parameter at a constant value of the Winkler

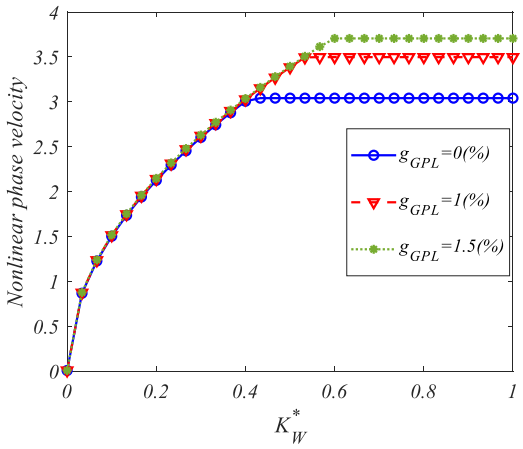


Figure 8. The impact of $K_W^*$ parameter and the GPL weight fraction on the structure's nonlinear phase velocity

coefficient. On the other hand, the nonlinearity phase velocity increases with the Winkler coefficient for each fixed value of the stiffness parameter. This indicates that the stiffness parameter and the elastic foundation's contribution to wave propagation are in competition. The trend of nonlinearity phase velocity decreasing with the stiffness parameter suggests that stiffer base structures might be able to suppress wave velocity, which ideally serves for vibration control in micro-scale devices. The results thus indicate a co-relationship between the Winkler foundation and the material in term of phase velocity. The engineers might make informed decisions on the combination of materials and supports that lead to the desired wave propagation character in the case of graphene-reinforced composites, according to the presented results.

Fig. 8 evaluates how the dimensionless Winkler coefficient influences the nonlinear phase velocity of the system with different amounts of graphene platelets. The x-axis shows the dimensionless Winkler coefficient, while the y-axis indicates the nonlinear phase velocity. The three curves plotted represent the weight fractions of graphene platelets at 0%, 1%, and 1.5%, respectively. The diagram shows that the increase of the Winkler coefficient leads to the increase of the nonlinear phase velocity, with the lower values area presenting a steeper slope and the higher values area exhibiting a plateau. It is noteworthy, however, that the highest weight fraction of graphene platelets is associated with greater nonlinear phase velocity at any Winkler coefficient value. This indicates that the effect of graphene on phase velocity is made even stronger by a stiffer elastic foundation. The interaction reveals that both material composition and foundation support are crucial factors in dynamic behavior and reliability of graphene-reinforced solar cell plates under nonlinear wave propagation optimization.

Fig. 9 shows how the nonlinear phase velocity varies as a function of the dimensionless Winkler coefficient for a few different ratios of the length scale parameter. The x-axis is the dimensionless Winkler coefficient, and the y-axis is the nonlinear phase velocity. The three lines represent length scale parameter ratios of 0, 0.5, and 1. The data imply that nonlinear phase velocity increases monotonically with the rise of both the Winkler coefficient and the length scale parameter ratio. Besides, for a specific value of the Winkler coefficient, the larger length scale parameter ratios result in higher nonlinear phase velocities. This phenomenon points out the size-

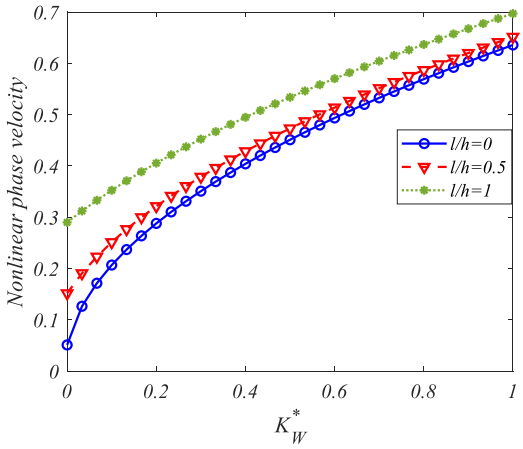


Fig 9. The impact of $K_W^*$, and $l/h$ parameters on the structure's nonlinear phase velocity

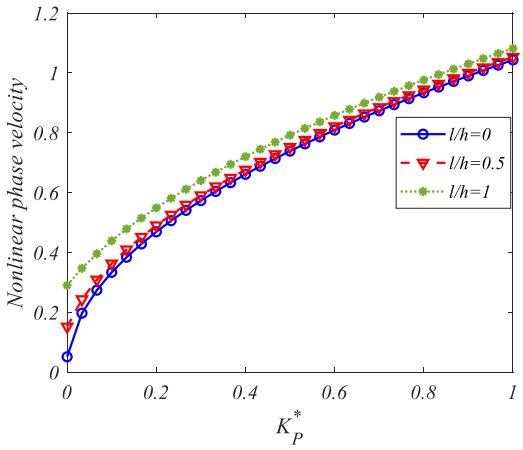


Figure 10. The impact of $K_P^*$, and $l/h$ parameters on the structure's nonlinear phase velocity

dependent effects in microstructured materials where the larger microstructural length scales can drive the elastic foundation's effect on the wave propagation. The synergy between these factors thus opens up a new avenue for the design and control of micro-sized solar cell plates with regard to their dynamic performance as well as structural reliability.

Fig. 10 illustrates how the length scale parameter ratio affects the nonlinear phase velocity, which in turn depends on the dimensionless Pasternak coefficient. The x-axis shows the dimensionless Pasternak coefficient, while the y-axis indicates the nonlinear phase velocity. The three curves plotted correspond to the different length scale parameter ratios of 0, 0.5, and 1. It is seen that the nonlinear phase velocity rises slowly with the increase of the dimensionless Pasternak coefficient in all instances. Moreover, the higher the length scale parameter ratio, the greater the nonlinear phase velocity increase at every Pasternak coefficient value, thus revealing the strong influence of microstructural size effects. The curves stay apart across the board, which means that the propagation characteristics are still very much influenced by the Pasternak foundation and the

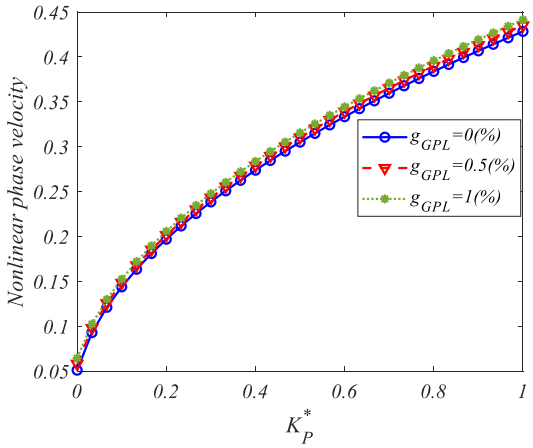


Figure 11. The impact of $K_P^*$ parameter and GPL weight fraction on the structure's nonlinear phase velocity

length scale effects. This phenomenon makes it imperative to take into account nonclassical continuum theories and microstructural parameters in the accurate forecasting and controlling of dynamic responses in graphene-reinforced composite plates, particularly for micro-scale solar cell applications where advanced vibrational performance is a necessity.

Fig. 11 illustrates how the nonlinear phase velocity is related to the dimensionless Pasternak coefficient for different amounts of graphene platelets. The horizontal axis represents the dimension less Pasternak coefficient, while the vertical axis represents the nonlinear phase velocity. The graph shows three curves for different percentages of graphene platelets, which are 0, 0.5, and 1%. It can be seen that the nonlinear phase velocity continues to increase uniformly with the dimensionless Pasternak coefficient for all the cases of graphene platelet content. Though there is an effect of the increase in the weight fraction of graphene plates on the nonlinear phase velocity, it is not very pronounced as the curves are so very close to each other. This means that the Pasternak foundation is completely contributing to the phase velocity increase while the graphene platelet content is merely a factor in this case. The results imply that in the cases where the Pasternak foundation effects are prominent, the microstructural reinforcement resulting from graphene platelets has a limited incremental effect which is very important for both material composition and foundation design in advanced solar cell plates.

Fig. 12 illustrates how nonlinear phase velocity varies in relation to the dimensionless Pasternak coefficient for different values of a stiffness-related parameter. The horizontal axis indicates the dimensionless Pasternak coefficient, while the vertical axis denotes the nonlinear phase velocity. The three curves correspond to parameter values 200, 400, and 600 related to wave number. Nonlinear phase velocity is increasing slowly but surely with the dimensionless Pasternak coefficient for all stiffness-related values. Higher stiffness parameter results in a slight increase in nonlinear phase velocity at each value of the Pasternak coefficient, yet the effect is not as strong as that of the Pasternak foundation itself. This trend indicates that while the base stiffness parameter influences the wave propagation dynamics, the dimensionless Pasternak coefficient is still the main factor in this case of enhancing phase velocity. The results indicate that foundation shear interactions are more effective in tuning dynamic properties than internal stiffness adjustments and thus are more important in the case of high-performance graphene-reinforced solar cell plates.

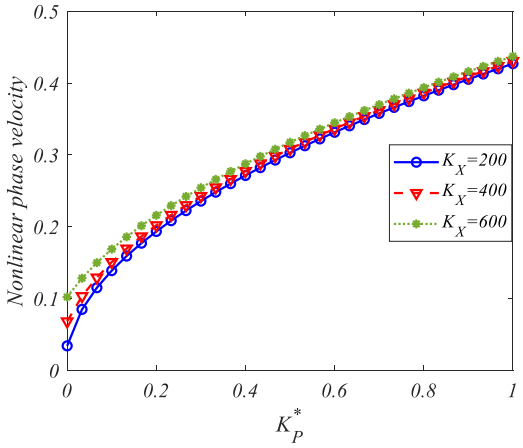


Figure 12. The impact of $K_P^*$, and $K_X$ parameters on the structure's nonlinear phase velocity

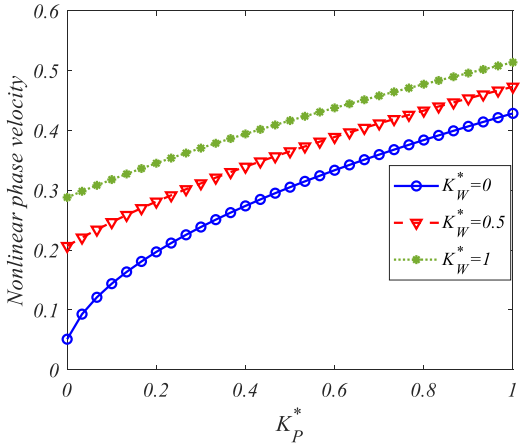


Figure 13. The impact of $K_P^*$, and $K_W^*$ parameters on the structure's nonlinear phase velocity

Fig. 13 presents how much the dimensionless Winkler coefficient affects the nonlinear phase velocity versus the dimensionless Pasternak coefficient. The horizontal line shows the dimensionless Pasternak coefficient, and the vertical line shows nonlinear phase velocity. The three lines are for the values of the dimensionless Winkler coefficient of 0, 0.5, and 1. The results indicate that the increase in the dimensionless Pasternak coefficient causes the nonlinear phase velocity to rise much higher than before, and this is further enhanced in a big way at the higher levels of the dimensionless Winkler coefficient. The difference in the curves becomes more and more pronounced as the Pasternak coefficient rises, which indicates a productive interaction of the two founding variables. Indicating this, one can see that normal and shear responses of the foundations must be accounted for in the modeling and controlling of wave propagation in graphene-reinforced composites. The findings underline the rich interaction that exists between the different parameters of the foundation, and this in turn is what determines the dynamic behavior of the micro-sized solar cell plates. This area is very critical as it will determine the design and optimization of the future solar technologies.

Table 4. Key parameters used in both the neural network and the genetic algorithm

| Parameter | Description | Value |
|---|---|---|
| Input Size | Number of input features | 6 |
| Output Size | Number of outputs | 3 |
| Number of Hidden Layers | Layers between input and output | 4 |
| Neurons per Hidden Layer | Number of neurons in each hidden layer | 64 |
| Activation Function | Nonlinear function applied at each neuron | ReLU |
| Population Size | Number of chromosomes in GA population | 20 |
| Number of Generations | Iterations of evolution | 50 |
| Number of Parents | Number of top performers selected as parents | 10 |
| Crossover Rate | Probability of crossover | 0.8 |
| Mutation Rate | Probability of mutation | 0.1 |
| Crossover Type | Method of combining parent genes | Single-point crossover |
| Mutation Type | Method of introducing random changes | Add small perturbations |
| Fitness Function | Inverse of loss function (MSE) | 1/MSE |
| Termination Criteria | Condition to stop GA evolution | Fixed number of generations |

### 6.3 The outcomes of the mentioned algorithm

Table 4 presents the main parameters utilized in the DNN-GA method for nonlinear wave propagation forecasting, which are applicable to both the neural network and the genetic algorithm. These parameters affect not only the architecture of the neural network but also the effectiveness of the optimization procedure.

### 6.4 Robustness and generalizability analysis of the DNN-GA model

In order to evaluate the reliability, applicability, and methodological rigor of the suggested DNN-GA model, a variety of supplementary analyses were performed in addition to the first performance metrics.

#### a) Data partitioning and cross-validation

The complete dataset comprising 15,000 samples produced by the mathematical model was divided into three separate portions: 70% for training (10,500 samples), 15% for validation (2,250 samples), and the remaining 15% for an independent test set (2,250 samples). In order to obtain a robust result and to lessen the impact of one random division, a 5-fold cross-validation was applied on the training and validation sets combined. The average $R^2$ score of all folds was $0.948 \pm 0.012$, and the average mean squared error (MSE) was $(4.21 \pm 0.45) \times 10^{-4}$, which means that the model's performance was consistent and there was little variance in predictions, as illustrated in Table 5.

#### b) Mitigating local minima convergence

The evolutionary property of the genetic algorithm part gives a strong protection against the possibility of the search getting stuck in shallow local minima. The search is done in such a way that it explores multiple areas of the parameter space at the same time through the combination of

Table 5. 5-Fold cross-validation results

| Fold | $R^2$ Score | Mean squared error (MSE) |
|---|---|---|
| 1 | 0.951 | $3.92 \times 10^{-4}$ |
| 2 | 0.937 | $4.88 \times 10^{-4}$ |
| 3 | 0.956 | $3.55 \times 10^{-4}$ |
| 4 | 0.942 | $4.63 \times 10^{-4}$ |
| 5 | 0.954 | $3.71 \times 10^{-4}$ |
| Mean $\pm$ Std | $0.948 \pm 0.012$ | $(4.21 \pm 0.45) \times 10^{-4}$ |

Table 6. Generalizability test across GPL patterns

| Training pattern | Test pattern | $R^2$ score | MSE |
|---|---|---|---|
| GPL-X | GPL-X (In-Pattern) | 0.941 | $4.15 \times 10^{-4}$ |
| GPL-X | GPL-O | 0.896 | $8.32 \times 10^{-4}$ |
| GPL-X | GPL-UD | 0.873 | $1.02 \times 10^{-3}$ |

keeping a population of candidate solutions (chromosomes) and the application of stochastic operators (crossover and mutation). The DNN-GA training was started with ten different random seeds to confirm this further. The final fitness values (1/MSE) and $R^2$ scores on the test set turned out to be in a close range ($R^2$: 0.939 - 0.942), which is a confirmation that the algorithm is finding a good solution quite near to the optimal one no matter how it was initialized.

### c) Out-of-distribution (OOD) predictions

The capability of the model to predict in areas outside its training circle was examined using OOD data. An additional data set was created with the wave number and length scale parameter ($l/h$) set to values that were 25% higher than the maximum and lower than the minimum of the training range. As predicted, there was a drop in the model's predictive accuracy and the average $R^2$ value fell to 0.782. This decline points to a major restriction of exclusively data-driven models when encountering new physical conditions and at the same time, it shows the benefit of physics-informed architectures in such extrapolation tasks.

### d) Generalizability across different GPL patterns

For the purpose of verifying generalizability, the DNN-GA model was fitted solely on the data corresponding to the GPL-X distribution pattern. Without retraining, it was then assessed using the test sets out of the GPL-O and GPL-UD patterns. The obtained results that are visible in Table 6 indicate a moderate decline in performance in comparison with the in-pattern test. The model still maintains good predictive capability ($R^2 > 0.87$), thereby, proving its power to grasp some of the mechanical relationships underlying the different distribution patterns, though, at the same time, confirming that it has partially learned some specific features of the pattern.

### e) Hyperparameter sensitivity analysis

Sensitivity analysis was carried out concerning four main hyperparameters, namely, the number of neurons per hidden layer, the population size for GA, the rate of mutation, and the number of training generations. The outcomes were expressed through the final $R^2$ score on the fixed test set

Table 7. Hyperparameter sensitivity analysis

| Hyperparameter | Tested Values | Optimal value | Impact on $R^2$ |
|---|---|---|---|
| Neurons/Layer | [32, 64, 128, 256] | 128 | High: Peaks at 128 |
| Population size | [10, 20, 50, 100] | 50 | Low-Med: Sat. at 50 |
| Mutation rate | [0.01, 0.05, 0.1, 0.2] | 0.1 | Medium: Optimal at 0.1 |
| Generations | [25, 50, 100, 200] | 100 | High: Requires >50 |

and the total training time and they are presented in Table 7. Model performance was extremely sensitive to the width of the network (neurons per layer) and the number of generations, with a saturation effect after certain thresholds. The mutation rate had an optimal mid-range value (0.1), with its lower and higher rates deteriorating performance. The parameter of population size had a less notable effect that was mainly confined to the minimum threshold, with bigger sizes leading to increased computational costs and yielding lesser returns.

## 7. Conclusion

In this paper, we carried out a detailed study of the nonlinear wave propagation in solar cells with graphene as a reinforcer and utilized a unique DNN–GA framework to corroborate and enhance the results for the first time. The investigation brings out the important role of graphene as a composite material with the ability to improve the mechanical and thermal properties of the composite materials, which would result in better performance of the solar cell of micro-size. The Halpin-Tsai model was used for forecasting the effective properties of graphene-containing composites, which laid down an important base for precise material modeling in studies dealing with nonlinear wave propagation. Theories like the modified coupled stress theory, sinusoidal shear deformation theory, and modified pair stress theory, when integrated together, provided us with the possibility of capturing the intricate characteristics of the material under the nonlinear loading. These theories facilitated a more precise depiction of the size-dependent influences and microstructural deformations taking place within the composite, which are vital for comprehending the material's reaction to external forces and its phase velocity characteristics. The use of Hamilton's principle in the process of governing equations made it possible to obtain an analytical solution, which provided a more thorough comprehension of the wave propagation mechanics in graphene-reinforced composites. The study's outcomes pointed out that the contribution of graphene reinforcement to the nonlinear phase velocity was considerable, thus it opened new ways for the understanding of the dynamic character of these materials in real-life scenarios. In addition, the DNN-GA framework was not only us but also was used in the study to provide the verification and optimization of results with great efficiency, ensuring the predictions are accurate and reliable. Thus, the research has made a breakthrough by creating a new path for the design and optimization of graphene solar cells, where the precise control over nonlinearity wave dynamics will be the key factor for improving the energy efficiency, mechanical stability, and performance. The study's findings will undoubtedly be the turning point for the field of materials science, especially in the area of next-gen renewable energy technologies. The methodologies and results outlined provide a trustworthy platform for subsequent research as well as the manufacture of next-gen solar cells with the participation of graphene-based composites in the leading role of solar energy application advancements.

## Acknowledgement

This work was supported by a research grant FRGS/1/2025/SS01/UKM/02/1 & GSB-2026-005 under the Ministry of Higher Education, Malaysia and UKM-GSB

## References

1. Verduci, R., Romano, V., Brunetti, G., Yaghoobi Nia, N., Di Carlo, A., D'Angelo, G., Ciminelli, C. (2022). Solar energy in space applications: review and technology perspectives. Advanced Energy Materials, 12, 2200125. https://doi.org/10.1002/aenm.202200125
2. Zhao, G., Hughes, D., Beynon, D., Wei, Z., Watson, T., Chung, W.T., Baker, J. (2024). Perovskite photovoltaics for aerospace applications− life cycle assessment and cost analysis. Solar Energy, 274, 112602. https://doi.org/10.1016/j.solener.2024.112602
3. Tu, Y., Wu, J., Xu, G., Yang, X., Cai, R., Gong, Q., Zhu, R., Huang, W. (2021). Perovskite solar cells for space applications: progress and challenges. Advanced Materials, 33, 2006545. https://doi.org/10.1002/adma.202006545
4. Xu, G., Cai, P., Tu, Y., Kong, H., Ke, Z., Li, Y., Zhuang, C., Du, X., Zhang, Y., Li, Z. (2024). Calibration for space solar cells: progress, prospects, and challenges. Solar RRL, 8, 2300822. https://doi.org/10.1002/solr.202300822
5. Peciak, M., Skarka, W., Mateja, K., Gude, M. (2023). Impact analysis of solar cells on vertical take-off and landing (VTOL) fixed-wing UAV. Aerospace, 10, 247. https://doi.org/10.3390/aerospace10030247
6. Zhang, L., Qiu, J., Cheng, H., Zhang, Y., Zhong, S., Shi, L., Yin, H., Tong, R., Sun, Z., Shen, W. (2024). Low-temperature Ta-doped TiOx electron-selective contacts for high-performance silicon solar cells. Solar Energy Materials and Solar Cells, 266, 112703. https://doi.org/10.1016/j.solmat.2024.112703
7. Tepner, S., Lorenz, A. (2023). Printing technologies for silicon solar cell metallization: a comprehensive review. Progress in Photovoltaics: Research and Applications, 31, 557-590. https://doi.org/10.1002/pip.3643
8. Di Sabatino, M., Hendawi, R., Garcia, A.S. (2024). Silicon solar cells: trends, manufacturing challenges, and AI perspectives. Crystals, 14, 167. https://doi.org/10.3390/cryst14020167
9. Wang, X., Xu, L., Ge, S., Foong, S.Y., Liew, R.K., Chong, W.W.F., Verma, M., Naushad, M., Park, Y.-K., Lam, S.S. (2023). Biomass-based carbon quantum dots for polycrystalline silicon solar cells with enhanced photovoltaic performance. Energy, 274, 127354. https://doi.org/10.1016/j.energy.2023.127354
10. Yu, J., Chen, Y., He, J., Bai, Y., Su, R., Cao, T., Liu, W., Chen, T. (2023). Enhancing poly-Si contact through a highly conductive and ultra-thin TiN layer for high-efficiency passivating contact silicon solar cells. Solar Energy Materials and Solar Cells, 260, 112491. https://doi.org/10.1016/j.solmat.2023.112491
11. Panagiotou, P., Tsavlidis, I., Yakinthos, K. (2016). Conceptual design of a hybrid solar MALE UAV. Aerospace Science and Technology, 53, 207-219. https://doi.org/10.1016/j.ast.2016.03.023
12. Wang, L., Liu, J., Li, Y., Wei, G., Li, Q., Fan, Z., Liu, H., An, Y., Liu, C., Li, J. (2024). Dislocations in crystalline silicon solar cells. Advanced Energy and Sustainability Research, 5, 2300240. https://doi.org/10.1002/aesr.202300240
13. Li, J., Kang, Q., Wang, Y., Zhou, Z., Sun, Z., Zhang, H., Lu, W., Tao, X., Zhang, S., Chen, X. (2024). Low oxygen content MoOx and SiOx tunnel layer based heterocontacts for efficient and stable crystalline silicon solar cells approaching 22% efficiency. Advanced Functional Materials, 34, 2310619. https://doi.org/10.1002/adfm.202310619
14. Trabelsi, A.B.G., Kaliyannan, G.V., Gunasekaran, R., Rathanasamy, R., Palaniappan, S.K., Alkallas, F.H., Elsharkawy, W., Mostafa, A.M. (2024). Surface engineering of SiO2-ZrO2 films for augmenting

power conversion efficiency performance of silicon solar cells. Journal of Materials Research and Technology, 28, 1475-1482. https://doi.org/10.1016/j.jmrt.2023.12.100
15. Lin, H., Wang, G., Su, Q., Han, C., Xue, C., Yin, S., Fang, L., Xu, X., Gao, P. (2024). Unveiling the mechanism of attaining high fill factor in silicon solar cells. Progress in Photovoltaics: Research and Applications, 32, 359-371. https://doi.org/10.1002/pip.3730
16. Li, Y., Chen, Z., Zhou, R., Zhao, W., Li, M., Chen, J., Huang, Z., Liu, J., Li, Y., Yang, M. (2024). Design of advanced porous silver powder with high-sintering activity to improve silicon solar cells. Nano Research, 17, 3189-3197. https://doi.org/10.1007/s12274-023-6339-x
17. Rabczuk, T., Areias, P., Belytschko, T. (2007). A meshfree thin shell method for non-linear dynamic fracture. International Journal for Numerical Methods in Engineering, 72, 524-548. https://doi.org/10.1002/nme.2013
18. Rabczuk, T., Gracie, R., Song, J., Belytschko, T. (2010). Immersed particle method for fluid-structure interaction. International Journal for Numerical Methods in Engineering, 81, 48-71. https://doi.org/10.1002/nme.2670
19. Rabczuk, T., Ren, H., Zhuang, X. (2019). A nonlocal operator method for partial differential equations with application to electromagnetic waveguide problem. Computers, Materials & Continua, 59, 31-55. https://doi.org/10.32604/cmc.2019.04168
20. Eshaghi, M.S., Anitescu, C., Thombre, M., Wang, Y., Zhuang, X., Rabczuk, T. (2025). Variational physics-informed neural operator (vino) for solving partial differential equations. Computer Methods in Applied Mechanics and Engineering, 437, 117785. https://doi.org/10.1016/j.cma.2024.117785
21. Liu, B., Wang, Y., Rabczuk, T., Olofsson, T., Lu, W. (2024). Multi-scale modeling in thermal conductivity of Polyurethane incorporated with Phase Change Materials using Physics-Informed Neural Networks. Renewable Energy, 220, 119565. https://doi.org/10.1016/j.renene.2023.119565
22. Fu, T., Wang, X., Rabczuk, T. (2024). Broadband low-frequency sound insulation of stiffened sandwich PFGM doubly-curved shells with positive, negative and zero Poisson's ratio cellular cores. Aerospace Science and Technology, 147, 109049. https://doi.org/10.1016/j.ast.2024.109049
23. Guo, H., Zhuang, X., Fu, X., Zhu, Y., Rabczuk, T. (2023). Physics-informed deep learning for three-dimensional transient heat transfer analysis of functionally graded materials. Computational Mechanics, 72, 1-12. https://doi.org/10.1007/s00466-023-02378-9
24. Safarpour, H., Safarpour, M., Jamali, J., Civalek, Ö. (2025). Sound radiation and phase velocity characteristics of FG bio-composite annular plates. Journal of Vibration Engineering & Technologies, 13, 366. https://doi.org/10.1007/s42417-025-01936-0
25. Guo, P., Zhang, Y., Xi, Y., Saleem, K., El-Meligy, M., Safarpour, H. (2024). Nonlinear transient deflections of multi-layer sector plate structures on auxetic concrete foundation: introducing an artificial intelligence algorithm for nonlinear problems. Structures, 70, 107563. https://doi.org/10.1016/j.istruc.2024.107563
26. Samaniego, E., Anitescu, C., Goswami, S., Nguyen-Thanh, V.M., Guo, H., Hamdia, K., Zhuang, X., Rabczuk, T. (2020). An energy approach to the solution of partial differential equations in computational mechanics via machine learning: concepts, implementation and applications. Computer Methods in Applied Mechanics and Engineering, 362, 112790. https://doi.org/10.1016/j.cma.2020.112790
27. Anitescu, C., İsmail Ateş, B., Rabczuk, T. (2023). Physics-informed neural networks: theory and applications. In: Machine Learning in Modeling and Simulation: Methods and Applications. Springer, Cham, Switzerland.
28. Ahmed, A., Uddin, M.N., Akbar, M., Salih, R., Khan, M.A., Bisheh, H., Rabczuk, T. (2023). Prediction of shear behavior of glass FRP bars-reinforced ultra-highperformance concrete I-shaped beams using machine learning. International Journal of Mechanics and Materials in Design, 20, 1-22. https://doi.org/10.1007/s10999-023-09684-3
29. Liu, B., Lu, W., Olofsson, T., Zhuang, X., Rabczuk, T. (2024). Stochastic interpretable machine learning based multiscale modeling in thermal conductivity of Polymeric graphene-enhanced composites. Composite Structures, 327, 117601. https://doi.org/10.1016/j.compstruct.2023.117601
30. Mortazavi, B., Zhuang, X., Rabczuk, T., Shapeev, A.V. (2023). Atomistic modeling of the mechanical

properties: the rise of machine learning interatomic potentials. Materials Horizons, 10, 1956-1968. https://doi.org/10.1039/D3MH00118C

31. Mortazavi, B., Shojaei, F., Shahrokhi, M., Rabczuk, T., Shapeev, A.V., Zhuang, X. (2022). Electronic, optical, mechanical and Li-Ion storage properties of novel benzotrithiophene-based graphdiyne monolayers explored by first principles and machine learning. Batteries, 8, 194. https://doi.org/10.3390/batteries8110194
32. Liu, B., Vu-Bac, N., Zhuang, X., Fu, X., Rabczuk, T. (2022). Stochastic integrated machine learning based multiscale approach for the prediction of the thermal conductivity in carbon nanotube reinforced polymeric composites. Composites Science and Technology, 224, 109425. https://doi.org/10.1016/j.compscitech.2022.109425
33. Safarpour, M., Rahimi, A., Alibeigloo, A., Bisheh, H., Forooghi, A. (2019). Parametric study of three-dimensional bending and frequency of FG-GPLRC porous circular and annular plates on different boundary conditions. Mechanics Based Design of Structures and Machines, 47, 1-31. https://doi.org/10.1080/15397734.2019.1662310
34. Wang, Y., Zeng, R., Safarpour, M. (2020). Vibration analysis of FG-GPLRC annular plate in a thermal environment. Mechanics Based Design of Structures and Machines, 48, 1-19. https://doi.org/10.1080/15397734.2020.1719508
35. Rahimi, A., Alibeigloo, A. (2020). High-accuracy approach for thermomechanical vibration analysis of FG-GPLRC fluid-conveying viscoelastic thick cylindrical shell. International Journal of Applied Mechanics, 12, 2050073. https://doi.org/10.1142/S1758825120500738
36. Wenham, S.R., Green, M.A. (1996). Silicon solar cells. Progress in Photovoltaics: Research and Applications, 4, 3-33. https://doi.org/10.1002/(SICI)1099-159X(199601/02)4:1<3::AID-PIP117>3.0.CO;2-R
37. Reddy, J.N. (2003). Mechanics of laminated composite plates and shells: theory and analysis. CRC Press, Boca Raton, FL, USA.
38. Akgöz, B., Civalek, Ö. (2015). A microstructure-dependent sinusoidal plate model based on the strain gradient elasticity theory. Acta Mechanica, 226, 2277-2294. https://doi.org/10.1007/s00707-015-1308-4
39. Song, M., Kitipornchai, S., Yang, J. (2017). Free and forced vibrations of functionally graded polymer composite plates reinforced with graphene nanoplatelets. Composite Structures, 159, 579-588. https://doi.org/10.1016/j.compstruct.2016.09.070